International Journal of Plasticity 26 (2010) 372–394

Contents lists available at ScienceDirect

International Journal of Plasticity

journal homepage: www.elsevier.com/locate/ijplas

Microstructure-sensitive extreme value probabilities for high cycle fatigue of Ni-base superalloy IN100

Craig P. Przybyla [a,b,*], David L. McDowell [b,c]

[a] Air Force Research Laboratory, Wright Patterson Air Force Base, OH 45433-7817, USA
[b] Georgia Institute of Technology, Materials Science and Engineering, Atlanta, GA 30332-0245, USA
[c] George W. Woodruff School of Mechanical Engineering, Atlanta, GA 30332-0245, USA

ARTICLE INFO

Article history:
Received 24 March 2009
Received in final revised form 29 July 2009
Available online 12 August 2009

Keywords:
High cycle fatigue
Ni-base superalloys
Extreme value statistics
Probabilistic fatigue
Microstructure-sensitive design

ABSTRACT

To quantify the effects of interactions between various microstructure attributes on fatigue life in the high cycle fatigue (HCF) regime, we have proposed a new microstructure-sensitive extreme value statistical framework. This framework couples the extreme value distributions of certain fatigue indicator parameters (FIPs) or response functions to the correlated microstructure attributes that exist at the extreme value locations of these FIPs. We demonstrate the application of this statistical framework to investigate the microstructure-sensitive fatigue response of the PM Ni-base superalloy IN100 at 650 °C. To accomplish this task, we construct statistical volume elements (SVEs) used to compute the local response for 200 instantiations of IN100. These SVEs are constructed and simulated via the finite element method with crystal plasticity constitutive relations. The results of the simulations are used to explore extreme value statistics of the FIPs for these microstructures. The extreme value distributions of the Fatemi–Socie FIP are fit with high confidence by the Gumbel distribution and are defined in a representative nature with as few as 25 simulated microstructure instantiations (i.e., SVEs). The extreme value marked correlation functions of the apparent Schmid factor based on the geometry of the slip systems relative to the loading direction indicate that cube slip may be important to fatigue crack formation in this material system. This supports previous experimental observations of fatigue crack formation and microstructurally small fatigue crack growth along cube planes in IN100 in grains that are unfavorably oriented for octahedral slip at elevated temperatures.

Published by Elsevier Ltd.

1. Introduction

Scatter in the high cycle fatigue (HCF) life of specimens or components depends on the extreme value probabilities of having existing hot spots or regions with increased local driving forces for fatigue damage formation (i.e., fatigue crack formation and microstructurally small crack propagation). Specifically, the probability of fatigue damage formation in a particular volume of material is established by the extreme value (i.e., rare event) probability of a particular existing combination of microstructure attributes that couple with the applied stress state such that fatigue cracks form and propagate. Coupling of microstructure attributes with loading conditions and the resulting fatigue response is the main source of both scatter and size effects in fatigue in the absence of other random environmental factors (e.g., temperature, atmosphere). As such, we commonly observe scatter in the fatigue response between multiple material volumes (or components) even when they

* Corresponding author. Address: Georgia Institute of Technology, Materials Science and Engineering, 771 Ferst Dr., Atlanta, GA 30332-0245, USA.
E-mail address: cpriz@gatech.edu (C.P. Przybyla).

0749-6419/$ - see front matter Published by Elsevier Ltd.
doi:10.1016/j.ijplas.2009.08.001

are fabricated from the same batch of processed material and tested in nearly identical environments. Although environmental effects can also contribute to the probability of surface to subsurface transition of crack formation, they are not considered in this particular work. The main emphasis of this work is on developing a consistent methodology to characterize correlations of microstructure attributes that exist with high probability relative to the nominal microstructure in regions where the fatigue driving forces are maximum (i.e., extreme value).

The dependence of fatigue damage formation on various microstructure attributes has been investigated extensively; several reviews have been published on the subject (Suresh, 1998; McDowell, 1996). For example, second phase inclusions or pores, large grains that are favorably oriented for slip, or grains adjacent to grains that are unfavorably oriented for slip have each been linked to fatigue damage formation in several metallic polycrystalline material systems. Identifying the underlying microstructure attributes that drive fatigue damage formation in material systems with multiple phases, complex processing histories, etc., however, is often complicated by the fact that multiple interacting microstructure features couple with the imposed cyclic plastic deformation and stress state to increase the local driving forces for fatigue damage formation. In most cases, this dependence cannot merely be deduced from direct quantitative image analysis of various microstructure attributes. Assessment of the coupling of microstructure attributes with the driving forces for fatigue damage formation requires a combination of experiments and computational simulation, along with a connective framework based on extreme value statistics.

In general, fatigue damage formation in polycrystalline metallic materials is primarily driven by irreversible slip on the scale of the microstructure. In addition, interacting microstructure attributes (e.g., grains, phases, inclusions, and voids) can increase local slip and associated driving forces for fatigue damage at the microstructure scale. In HCF, where stress amplitudes remain below the macroscopic flow stress and cyclic plasticity is quite heterogeneous, fatigue lives are dominated by fatigue damage formation rather than by physically small or large crack propagation (cf. McDowell, 1997, 1999; Miller, 1991, 1993). Accordingly, the emphasis is placed on cyclic plasticity-based fatigue indicator parameters (FIPs) that reflect probability of microstructure scale crack formation and microstructurally small crack growth.

For most applications, large numbers of experiments are necessary to meaningfully quantify any variability in fatigue life and to identify any change in the mechanism of fatigue damage formation as a function of applied loading conditions for a given specimen size. Typically, insufficient experimental data are available to support this quantification. Moreover, the mathematical form of the tails of the probability distributions for the driving forces for fatigue damage formation, such as the local distributions of stress/strain, are not well characterized; moreover, the dependence of the character of those tails on single and/or interacting microstructure attributes are not well understood.

In this work, we are primarily concerned with how the crystallographic attributes of a polycrystalline microstructure (e.g., grain orientation, disorientation, size, and shape distributions) affect local driving forces for fatigue crack formation and early growth in HCF. In general, plastic strain inhomogeneity at the grain level in polycrystals subjected to cyclic loading is directly linked to crystallographic texture. Winter et al. (1981) observed that plasticity occurs preferentially in grains having slip systems with high Schmid factors, with slip localized within slip bands. Using crystal plasticity simulations to calculate distributions of cyclic slip in polycrystals, Bennett and McDowell (2003) demonstrated that distributions of slip could be quite heterogeneous in HCF. This heterogeneity is directly related to complex interactions between grains of differing orientations. Sauzay and Jourdan (2006) explored these types of interactions between grains by computationally characterizing the distributions of elastic stress fields around grain clusters at the free surface using elastic FE simulations. They predicted that grain interactions could affect the local resolved shear stress by as much as 18% in copper and austenitic stainless steels depending on the local orientations of the neighboring grains. Inhomogeneity of elastic stress fields corresponds to localization of plastic strain in regions of stress concentration associated with the jump of the elastic stiffness across grain boundaries and compatibility requirements of the polycrystal. Specifically, we will consider the effects of local crystallography (e.g., phase, grain orientation, grain disorientation, grain topology, etc.) on slip in a powder metallurgy (PM) Ni-base superalloy, IN100.

Ni-base superalloys are predominantly used in aircraft gas turbine engines due to their high strength and creep resistance at high temperatures that is conferred by coherent γ' Ni_3Al precipitates of $L1_2$ face-centered cubic (fcc) structure. These precipitates are dispersed in the γ austenitic Ni solid solution matrix of fcc crystal structure and provide excellent resistance to slip. Commonly, fatigue damage formation in polycrystalline superalloys has been linked to the existence of large pores or non-metallic inclusions introduced during processing. Often, inclusions debond from the matrix or crack during primary forming processes. During loading, the stress concentrations at inclusions/pores often lead to the formation of fatigue cracks (Hyzak and Bernstein, 1982; Goto and Knowles, 1998; Pang and Reed, 2003). However, as processing techniques improve, cleaner Ni-base superalloys are being developed that have lower number density of inclusions/pores; consequently, fatigue cracks are increasingly observed to form along crystallographic planes. For example, Jha et al. (2005) noted that subsurface fatigue crack formation occurs in individual grains absent of any voids/inclusions in René 88DT, particularly at lower stress amplitudes (i.e., in the HCF regime). In this case, the nucleation region associated with the size of the crystallographic facets at the sites of fatigue crack formation was observed to be much larger than the average grain size. This suggests that cracks tend to form in larger grains. In the same alloy, Shyam et al. (2004) noted that cracks form predominantly in larger grains or at inclusions near large grains. Additionally in René 88DT, Miao et al. (2007) also observed that most critical (i.e., life-limiting) fatigue cracks in the HCF/VHCF regime initiate crystallographically away from the surface. The grains in which these cracks form were observed to be large in size relative to the average grain size. Here these grains were associated with higher Schmid factors, indicating they are oriented favorably for slip. Others have shown that slip bands associated with shearing of

the second phase γ' precipitates and subsequent fatigue damage formation have been observed to be more common in coarser grained superalloys, while deformation in the smaller grains has been observed to be more homogeneous (Antolovich and Jayaraman, 1983; Lerch et al., 1984).

The analysis of the slip character in Ni-base superalloys has provided some insight into fatigue damage formation in these materials systems. As mentioned previously, the γ austenitic phase in these Ni-base superalloys has an fcc crystalline lattice. As typical in fcc materials, slip is expected on the 12 octahedral $\{1\,1\,1\}\langle 1\,1\,0\rangle$ slip systems. However, contributions of an additional six cube $\{1\,0\,0\}\langle 1\,1\,0\rangle$ slip systems have been observed in the γ phase in many Ni-base superalloys at certain elevated temperatures in the form of macroscopic slip traces (Bettge and Österle, 1999). Although limited cube slip is possible in the Ll_2 ordered γ' phase, it is not commonly considered as likely to occur in the austenitic γ phase. Through detailed investigation using transmission electron microscopy (TEM), Bettge and Österle (Bettge and Österle, 1999), have postulated that this cube slip along $\{1\,0\,0\}$ *planes* is actually due to the "zig-zag" cross slip of screw dislocations on $\{1\,1\,1\}$ planes when blocked at the γ/γ' interfaces, as depicted in Fig. 1. As these dislocation migrate within the channels between γ' precipitates, they create macroscopic $\{1\,0\,0\}$ slip traces.

Cube slip has been observed in several single crystal Ni-base superalloys over a wide range of temperatures. For example, Miner et al. (1986) investigated slip traces in single crystal of René N4 at room temperature, 650 °C, 760 °C, 870 °C, and 980 °C. They observed slip traces along $\{1\,0\,0\}$ planes for all the temperatures considered when the crystals were oriented with the $\{1\,1\,1\}$ slip planes perpendicular to the loading direction. Additionally, at increasingly higher temperatures, $\{1\,0\,0\}$ slip traces were observed with increasing frequency in the crystals oriented in directions other than $\langle 1\,1\,1\rangle$ relative to the loading direction. Effectively, cube slip accommodates deformation for grains in "hard" crystallographic orientations. At 870 °C $\{1\,1\,1\}$ slip traces were only observed for crystals oriented near $[0\,0\,1]$ and $[0\,1\,1]$ and all others were of $\{1\,0\,0\}$ character. Bettge and Österle (1999) observed "zig-zag" cube slip in single crystals of SC16 oriented with the $\{1\,1\,1\}$ slip planes perpendicular to the loading direction. Westbrooke et al. (2005) observed slip bands traces along $\{1\,0\,0\}$ planes in single crystals of a Pratt and Whitney alloy for a crystal with unfavorable orientation relative to slip on $\{1\,1\,1\}$ planes and octahedral slip for a crystal oriented for loading in the $[1\,\bar{1}\,0]$ direction. They also observed slip traces for the crystal tested in the $[1\,0\,0]$ direction that were neither of $\{1\,1\,1\}$ or $\{1\,0\,0\}$ character. The morphology and distribution of γ' appears to dictate the character of slip in these types of superalloys. For example, Nitz et al. (1998) examined slip in single crystals of NIMONIC 105 at temperatures from 10 °C to 877 °C via TEM analysis and only observed octahedral slip. We note that in this particular material the γ' precipitates are small relative to the other materials discussed here ($\sim$17 nm) and are spherical in their morphology whereas in most single crystals the γ' precipitates are an order of magnitude larger and tend to have a cuboidal morphology. The slip character of these single crystals is summarized in Table 1.

Various slip modes have also been observed in fatigue tests of various polycrystalline Ni-base superalloys. The slip behavior of various polycrystalline alloys is summarized in Table 2. Generally in these alloys fatigue cracking propagates along $\{1\,1\,1\}$ planes at lower homologous temperatures and along $\{1\,0\,0\}$ planes at moderate temperatures (i.e., between 500 °C and 800 °C). We point out that this is what was observed in fatigue tests of IN100 (Li et al., 2004). In contrast, when the γ' precipitates are more spherical and smaller in size and have lower volume fraction, slip and cracking along $\{1\,0\,0\}$ planes has not been observed, such as in René 88DT (Miao et al., 2008).

Statistical treatments of fatigue have primarily been based on large numbers of experiments. Typically, one observes a wide range of scatter for a given component in the number of cycles to failure, particularly in HCF. For example, in Fig. 2 we can see significant variability in the overall fatigue lives in IN100 across a range of applied stress magnitudes (Jha et al., 2008). The variability of fatigue life is assessed by extensive experimentation to obtain a statistically significant sample. Designers then use these data to predict component life with an acceptable level of risk. Such data collection requires significant time and resources and does not necessarily provide understanding of the mechanism(s) involved in dictating variability. In addition, the resulting predictions often change with sample size. The problem is further complicated when multiple mechanisms of damage formation are observed (Jha et al., 2005, 2007, 2008). In these cases, multiple competing mechanisms of fatigue damage formation and fatigue crack growth make it difficult to accurately predict fatigue life because different mechanisms operate at different stress magnitudes and often microstructure attributes vary spatially in the material. For example, multiple modes of failure are evident in the cumulative probability plot in Fig. 2(b) at the stress magnitude

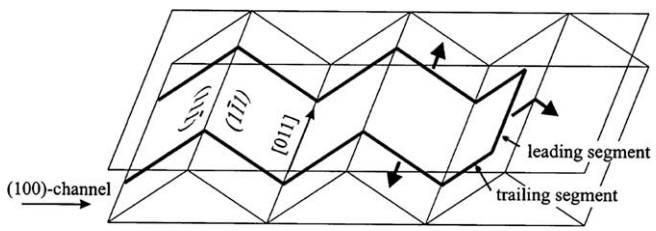

Fig. 1. Schematic of zig-zag $\{1\,1\,1\}$ slip in the $\{1\,0\,0\}$ channels. Thick arrows indicate the directions of the dislocation segments. The $[0\,0\,1]$ direction is the intersection line of the $\{1\,1\,1\}$ planes and is parallel to the Burgers vector of the dislocation loop $\vec{b} = 1/2[0\,0\,1]$. Figure from Bettge and Österle (1999). Reprinted with permission.

Table 1
The slip character of several different single crystal Ni-base superalloys.

Material	Volume fraction γ'	Average size of γ' (nm)	γ' shape	Temp. (°C)	Strain rate (s^{-1})	Slip character	Ref.
René N4	0.65	250	Cuboidal	RT, 650, 760, 870, 980	1–2.5×10^{-5}	[1 1 1] oriented crystals exhibited {1 0 0} slip traces at all temperatures and range of orientations exhibiting {1 0 0} slip traces (instead of {1 1 1}) increased with temperature	Miner et al. (1986)
NIMONIC 105	0.47	17.2	Spherical	10–877	7×10^{-5}, 1.4×10^{-4}	No observed {1 0 0} slip traces, only {1 1 1} type	Nitz et al. (1998)
SC16	0.35, 0.05	450, 80	Cuboidal	650, 750, 850	10^{-5}	Observed slip traces on {1 0 0} planes at 650 °C and 750 °C for ⟨1 1 1⟩ oriented crystals	Bettge and Österle (1999)
Heat treated PW alloy	0.51	500	Cuboidal	RT	10^{-5}	[1 1 0] oriented crystals exhibited {1 1 1} slip traces, [1 1 1] oriented crystal exhibited {1 0 0} slip traces and [1 0 0] oriented crystals exhibited neither	Westbrooke et al. (2005)

of 1150 MPa. In this case, the authors assert that the bi-modal nature of the failure probability relates to the fact that there exist two different competing failure mechanisms (Jha et al., 2008).

Processes of HCF crack formation and early growth depend on a few key attributes (or sets of attributes) such as the largest inclusion or void within an entire population of such features. There is significant scatter in experimentally measured HCF life because attributes that govern failure lie within the tails of joint distributions of attributes and responses, necessitating consideration of extreme value statistics. For example, if the key feature of the fatigue life in a particular material is determined by the largest inclusion of a certain type, an understanding of the distribution of inclusion sizes in the critically stressed regions would be essential to modeling the HCF life for that particular material.

The problem of the largest inclusion size in clean steels has been considered by several different workers and is summarized in a review by Atkinson and Shi (2003). In this case, different models exist that predict the fatigue resistance of these steels based on the largest inclusion size. Specifically, these models predict the maximum inclusion size using an assumed log–normal distribution, statistics based on the extreme value distribution function of Gumbel (1958), or a statistical method based on the Generalized Pareto Distribution (GPD). All of these methods, however, assume failure based on a single attribute (e.g., inclusion size) and do not consider how interacting attributes affect the damage processes of interest. For example, in many cases the driving forces for damage formation around an inclusion might depend as much on the orientation of the grains that affect the local slip processes in the matrix around an inclusion as on the size of the inclusion itself. We also argue that a framework that only considers purely geometric attributes such as inclusion size, grain size, or grain orientation is in general insufficient to quantify the scatter in HCF life. The additional attribute(s) of material response (e.g., stress, strain, plastic strain and other driving force parameters) coupled with geometric attributes of microstructure facilitate pursuit of joint statistics of extreme value type that are relevant to minimum fatigue life design.

Table 2
The slip character of several different polycrystalline Ni-base superalloys. Because in many cases the volume fraction of the γ' precipitates was not reported, we list the combined weight % of Al + Ti which are the limiting components for the formation of the γ' precipitates.

Material	Grain size (μm)	Wt% Al + Ti	Volume fraction γ'	Average size of γ' (nm)	γ' shape	Temp. (°C)	Slip character	Ref.
MARM 004	nr	10.55*	0.5	~1000	Cuboidal	RT, 600	Facets on {1 1 1} at RT and facets on {1 0 0} at 600 °C	Vincent et al. (1981)
NIMONIC AP1	40–50	7.4	nr	500	Cuboidal	RT	Most cracking on {1 1 1}, but cracking on {1 0 0} observed when slip is limited to single grains	King (1981)
Udmit 700	nr	7.5	nr	200	Cuboidal	RT, 850	Crack growth observed only on {1 0 0} planes at both RT and 850 °C	Sadananda and Shahinian (1981)
IN100	30	10.2	0.6**	~1000	Cuboidal	RT, 538	At RT cracks form on {1 1 1} and at 538 °C cracks form on {1 0 0}	Li et al. (2004)
René 88DT	26	5.8	nr	100–200	Spherical	593	Cracks form and propagate along {1 1 1} planes	Miao et al. (2008)

* For this material we report the combined wt% of Al + Nb + Ta which are in this case the limiting components for the formation of the γ' precipitates.
** Although this value was not reported in the paper it was given by the authors who wrote this paper. Values not reported in the respective references are listed as "nr" for not reported.

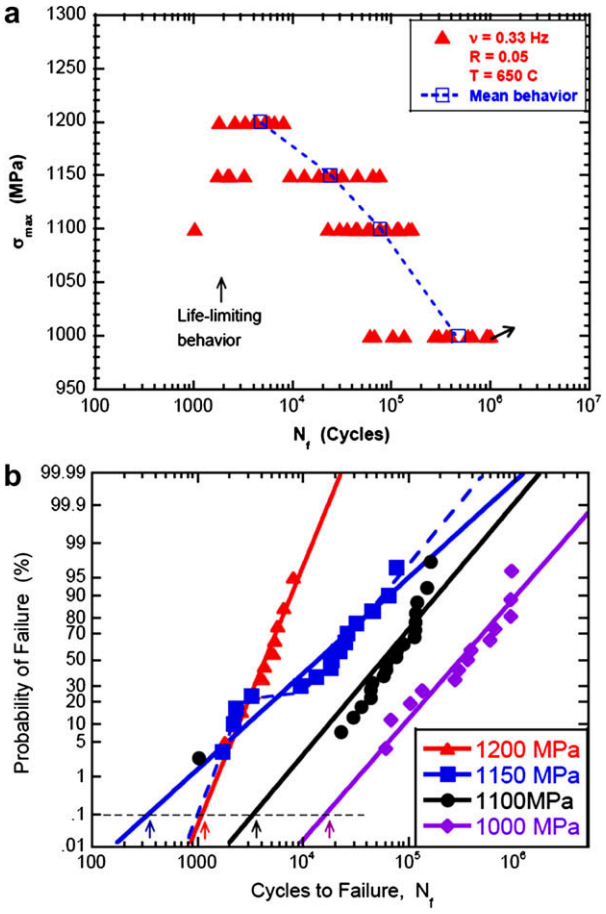

Fig. 2. The fatigue variability of IN100 from physical fatigue testing at various stress magnitudes: (a) mean versus life-limiting behavior and (b) cumulative distribution functions for tests at different stress magnitudes. Figure from Jha et al. (2008). Reprinted with permission.

In the present work, we propose a new statistical framework that links extreme value probabilities of various response parameters to the correlated microstructure attributes associated with the extreme value response. Here we exercise this statistical framework using computational simulations that estimate the cyclic deformation response in a Ni-base superalloy IN100 at 650 °C using a crystal plasticity formulation implemented using the finite element (FEM) method. Finally, we compare our results to a limited number of fatigue experiments available in the literature for this particular material system.

2. Methodology

2.1. Extreme value marked radial microstructure correlation functions

The objective is to develop a statistical framework that is able to quantify the coupling of the extreme values of certain FIPs to the key microstructure attributes that are associated with these extreme value response parameters. To achieve this objective we postulate that our proposed statistical framework must meet three primary requirements:

1. It must contain information regarding both the distributions of microstructure attributes and potential interactions or correlations between multiple microstructure attributes.
2. It must link the distributions of microstructure attributes and correlations between various microstructure attributes to distributions of local response parameters (e.g., FIPs).
3. It must be able to address the extreme value nature of fatigue crack formation and early growth scenarios.

We propose a two component statistical framework to satisfy these requirements. Given a spatial window Ω, we define the probability distribution of the extreme value response parameter α as $F^{ex}(\alpha|\Omega)$, which is associated with the probability that the response parameter of value α is the extreme value for a sampled statistical volume element of microstructure Ω. The extreme value response parameter could be defined by a number of different responses such highest associated stress,

strain, or plastic strain magnitude averaged over grain sized volumes, for example. This form of the extreme value distribution follows the ideas of extreme value (or importance) sampling from the classical extreme value statistics of Gumbel (Gumbel, 1958; Castillo, 1988). The basic procedure to construct such a distribution is to sample the extreme/minimum value parameter of interest across a number of samples in time and/or space. The classical example of Gumbel (1958) is to generate a distribution of maximum river depths by determining the maximum river depth over a defined stretch of river each year for a number of years. Similarly, in this work we consider the distribution of the maximum response parameters by sampling the maximum response in a number of equal volumes sampled from the bulk material (i.e., entire microstructure ensemble).

To also characterize the statistical influence that certain interacting microstructure attributes (e.g., grain size, grain orientation, grain misorientation, phase) have on the extreme value distributions of response, we define a new extreme value marked correlation function. For example, we define the extreme value marked radial correlation function $R^{\max(\alpha)}(\beta, \beta'|r, \Omega)dr$ as being associated with the probability of finding of a sphere centered at the microstructure attribute β coincident to the location of the maximum response parameter α in the microstructure window Ω, with microstructure attribute β' at a distance within r to $r + dr$ from β in any direction. Similar extreme value marked correlation functions could be constructed for n-point correlation functions, nearest neighbor distribution functions, lineal path correlation functions, etc. Although this newly introduced extreme value marked correlation function is based on the notion of the marked correlation functions introduced by Pyrz (1994), this new construct is fundamentally unique in its framing of extreme value statistics. In this work, we use the form of the extreme value marked radial correlation function as it was just introduced. We note that radial correlation functions do not contain information regarding anisotropy in the morphology of the specific microstructure attributes considered. These radial correlation functions, however, do describe the correlation lengths between the specific microstructure attributes being considered without regard to directionality, which is of primary interest in this work.

These coupled statistical parameters capture both the extreme value response of the microstructure as represented by the response parameter α and the biased correlations of microstructure attributes between β and β' in the neighborhood of the observed extreme values of α in a microstructure window Ω. In this way, spatial correlations are identified between microstructure attributes that have a high probability of existing in the neighborhood of an extreme value response parameter. This sampling is performed over the microstructure window defined by Ω and is expected to depend on the size of Ω. Multiple instantiations of Ω are required to effectively characterize both $F^{ex}(\alpha|\Omega)$ and $R^{\max(\alpha)}(\beta, \beta'|r, \Omega)$ to build up the tail of the probability distribution corresponding to extreme value response neighborhoods. The present framework facilitates comparison among multiple microstructures for a given material or comparison of significant microstructure attributed being considered in the sampling different materials which can support materials design.

Constructing the extreme value distribution with the corresponding extreme value marked correlation function requires a significant number of simulations/experiments if they are to be considered statistically meaningful. This can require extensive processing time for both simulations and data analysis depending on the complexity of the models being analyzed. The number of samples required depends on the response parameter considered and material being analyzed. Analogous experimental data are not typically available and are very expensive to obtain. Typical fatigue experiments will not provide enough information to construct these coupled distribution functions because such experiments consist of only a few data points at each stress/strain amplitude considered. In addition, experimentally, fatigue hot spots are identified after failure and characterization of the sites of fatigue damage formation and their neighborhoods is very cumbersome and typically requires destructive sectioning. Thus, although this proposed framework is general in its application to experiments and/or simulations, we envision that it will be much more practically applied to simulations that are substantiated with limited experimentation.

2.2. Simulation strategy

To exercise the foregoing extreme value statistical framework for polycrystalline Ni-base superalloys, we choose a strategy that estimates the proposed statistical parameters via the simulation of multiple microstructure instantiations. Specifically, we examine the influence of polycrystalline microstructure on probability of crystallographic fatigue crack formation in the Ni-base superalloy IN100. We recognize that fatigue damage formation in this particular material system primarily relates to the presence of non-metallic inclusions and/or pores. However, we have noted that Ni-base superalloys have been developed with much smaller populations of these types of inclusions/voids that do fail predominantly crystallographically (e.g., Miao et al., 2008). Thus, in this work we are exploring how this variant of IN100 would fail crystallographically in the absence of non-metallic inclusions or voids. In addition, the improved understanding of extreme value behavior of the orientation dependent slip processes in IN100 developed here can later be coupled with the existence of inclusions/voids to better current predictive models of fatigue crack formation in this material system. To accomplish this objective, digital representations of microstructures are simulated via the FE package ABAQUS (2007) coupled with a microstructure-sensitive crystal plasticity model for IN100 (Shenoy et al., 2007, 2008).

We briefly describe the crystal plasticity model for IN100. Generally superalloys are more complex to model because of their tension–compression asymmetry and the non-Schmid characteristics of the Ni_3Al phase due to dislocation core spreading effects. The grain size of the primary γ phase along with the size and spacing of the coherent γ' precipitates can greatly affect the material response of these material systems. For example, dislocation mechanisms change from precipitate shearing to bypassing by Orowan looping depending on the spacing, size and volume fraction of the γ' precipitates, as well as the

amplitude of applied strain. In this model (Shenoy et al., 2007, 2008), the precipitates are not explicitly modeled, but the influence of primary, secondary and tertiary γ' precipitates are included through certain internal state variables. Also incorporated in the model are the average effect of the grain size on the constitutive response and the dependence of the flow stress on crystallographic orientation. Shenoy et al. (2007, 2008) consider both the standard 12 octahedral $\langle 1\ 1\ 0\rangle\{1\ 1\ 1\}$ slip systems and six cube slip systems $\{1\ 0\ 0\}\langle 1\ 1\ 0\rangle$. As previously mentioned, the cube slip systems describe "zig-zag" octahedral slip that has been observed at the γ–γ' interface in the γ matrix and cube slip that occurs in γ' precipitates at higher homologous temperatures for crystals in "hard" orientations for octahedral slip. This particular model has been calibrated for IN100 at 650 °C. Appendix A lists the constitutive model equations and parameters relevant to response at 650 °C; more details regarding definition of various terms can be found in Shenoy et al. (2007, 2008).

2.3. Digital microstructure models

Using a crystal plasticity formulation allows these digital microstructure volumes to be statistical volume elements (SVEs) for local plasticity response (a key driving force for fatigue damage formation). Each statistical volume element for a desired response (i.e., grain scale plasticity) is designed to be large enough such that the response parameter of interest at a particular location is unaffected by statistical variations in the microstructure at distances on the order of the size of the volume (i.e., correlation length is less than size of SVE); however, the volume is not so large that it contains a statistically representative set of responses for that particular response parameter. This is in contrast to a representative volume element (RVE) that is defined such that the distribution of local response or effective response of the volume will not change based on where the RVE is sampled from the microstructure ensemble (i.e., bulk material), or if it is further increased in size. In some cases, information obtained from multiple SVEs can constitute a RVE level characterization. We note, however, that it is sometimes the case that for a particular response a RVE of reasonable size is unattainable. This is particularly true when trying to capture extreme value distributions of microstructure response that affect rare event damage formation and growth. This implies that complete characterization of the tail of the probability distribution function (PDF) for fatigue response requires a very large RVE.

In the present case, we seek to simulate multiple SVEs of sufficient size such that the lower order moments of the cyclic plasticity response on the scale of the grains are unaffected by further increasing the volume of the SVE. Of course, the higher order moments affect the tail of the PDF and the RVE size for invariance of these moments would be quite large, in general. We also desire that the SVE be suitably large to serve as a RVE in terms of the overall effective (i.e., macroscopic) elastic/plastic response. In other words, we want the stress–strain response taken from any microstructure instantiation to be representative of any other. The RVE for this effective response is insensitive to the higher order moments of the slip distribution, and is not the same as a RVE for the extreme value distribution of FIPs. This construct follows the same ideas behind SERVEs as defined by Swaminathan and Ghosh (Swaminathan et al., 2006; Swaminathan and Ghosh, 2006). Being able to simulate variations in the local response via these types of SVEs enables us to computationally explore how microstructure heterogeneity affects fatigue variability.

A Voronoi tessellation is a mathematical construct that describes a space partitioned around predefined centers such that all points closer to a given center than any other is associated with that center. In this manner, the space is divided up into a set of space filling convex polyhedral. Voronoi tessellations have been used in many different applications and the geometrical concept behind this construction is well defined in the literature (Aurenhammer, 1991). Fast Voronoi generation algorithms are readily available (Barber and Huhdanpaa, 2003). Gross and Li (2002) evaluated Voronoi tessellations based on structure, topology and statistics relative to typical polycrystalline materials and observed that both topology and various statistical properties do not agree well with those measured experimentally. They suggest that more realistic Voronoi tessellated models for polycrystalline materials can be generated using optimization methods to randomly perturb the centroids of the Voronoi tessellated cells to match certain statistical distributions measured from actual material systems like grain size, grain volume, grain boundary length, etc. It was also suggested that optimization methods could be used to match various texture measurements such as orientation or misorientation/disorientation (cf. Randle, 2003). Modifying random Voronoi tessellations to match more realistic distributions of grain size has also been performed earlier by others (Barbe et al., 2001a,b) to create RVEs for FE simulations. Recently, Zhang et al. (2006, 2007) used modified Voronoi tessellations that were optimized with a simulated annealing algorithm to fit experimentally characterized statistics of orientation, disorientation, and phase volume fraction in multiphase Ti–6Al–4V to construct FE models for crystal plasticity simulations. Additionally, Shenoy et al. (2007) constructed digital microstructure instantiations for IN100 using the same methods. Similar algorithms are used here to fit distributions of grain size, orientation and disorientation to construct SVEs for IN100. A SVE generated for IN100 along with an imposed voxellated mesh can be seen in Fig. 3. The target and optimized distributions for the grain volume normalized by the target average grain volume are given in Fig. 4.

The microstructures simulated in this work are constructed via a C++ computer program that generates these statistical volume elements of realistic polycrystalline microstructures. The actual Voronoi tessellation is computed using QHULL (Barber and Huhdanpaa, 2003) (see http://www.qhull.org). The simulated polycrystalline microstructures are generated using this modified Voronoi tessellation algorithm such that all points closer a grain center than any other grain center, belong to that grain. An additional parameter is also input by the user that defines the ratio of the minimum distance between any two grain centers to average distance between the grain centers. This prevents grain centers lying too close, thus also preventing the generation of very small Voronoi cells (i.e., grains). Fitting the simulated distributions of grain size, grain

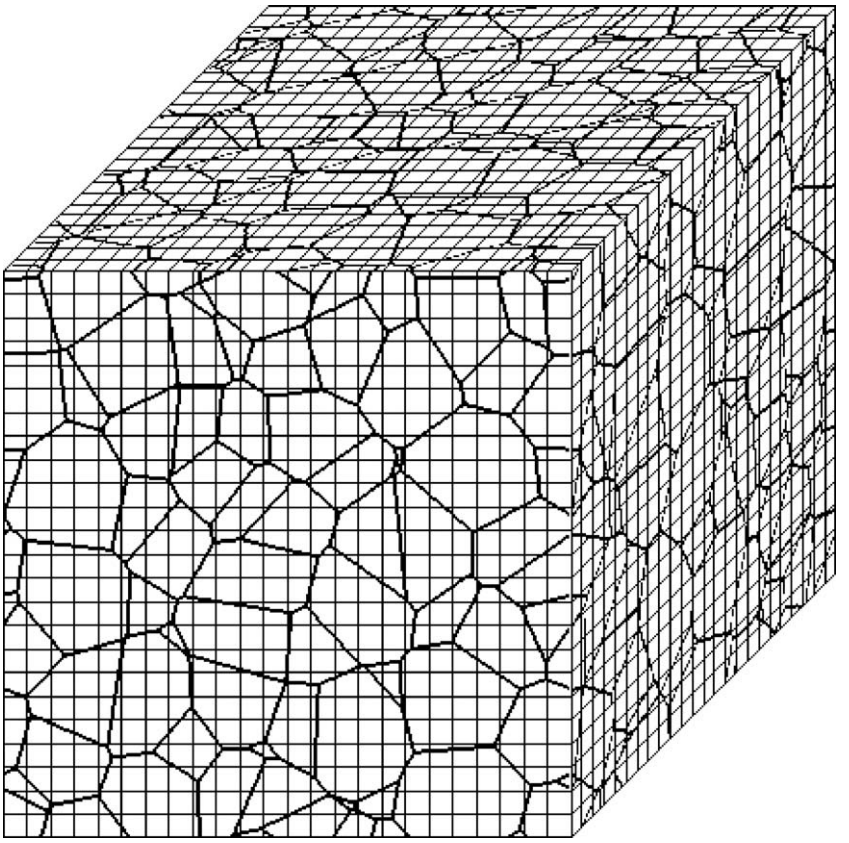

Fig. 3. SVEs generated via the Voronoi tessellation based microstructure generator for IN100 with associated FE mesh. Note that the meshes are voxellated and do not exactly correspond to the boundaries as defined by the Voronoi tessellation.

orientation, and grain disorientation is performed in the same manner as demonstrated previously by others (Shenoy et al., 2007; Zhang et al., 2006, 2007). In our case, we chose a random orientation distribution function (as commonly observed in IN100) and a random Mackenzie disorientation distribution function (Mackenzie, 1958; Mackenzie and Thompson, 1957).

Once a microstructure volume or instantiation is constructed and optimized to fit the target distributions of grains size, grain orientation, and grain disorientation, the program writes the ABAQUS input files that contain all the necessary information to simulate the microstructures. Information in these input files includes the details of the geometry, mesh and

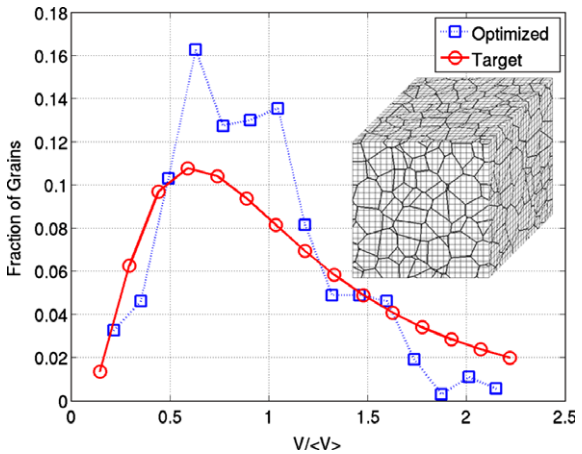

Fig. 4. The target and optimized grain size distribution of a SVE generated for IN100 where V is the actual grain volume and $\langle V \rangle$ is the target average volume or 8.0×10^{-6} mm^3 or a cube root grain size of $\sim$0.02 mm.

boundary and loading conditions. The initial simulation cell geometry is defined by the user defined values of edge length and mesh density (the number of elements along each edge of the simulated block of microstructure). The user also defines the target distributions for the grain size, grain orientation and grain disorientation. Once the global simulation cell geometry is generated (with grain centers defined), the elements and nodes are created based on the mesh density input by the user. Using the known edge length and mesh density, the element edge length and total size is calculated. The elements are constructed as an array of cuboidal elements (type C3D8R in ABAQUS) each with identical dimensions. These particular elements employ reduced integration to speed up computation time. Cuboidal elements are also convenient because the overall simulation cell was assumed to be cubic in this model. In addition, a voxellated mesh greatly simplifies the application of periodic boundary conditions in all directions.

2.4. Microstructure attributes and fatigue indicator parameters

The strain-life approach in fatigue has been applied mainly in the low cycle and transition fatigue regimes; however, microplasticity (i.e., heterogeneous plasticity at the scale of microstructure) is relevant to understanding fatigue crack formation and early crack propagation in HCF (McDowell, 1996, 1999). Coffin (1954) and Manson (1954) independently proposed a power law correlation of plastic strain amplitude, $\Delta\varepsilon_p/2$, with the number of cycles, N_f, to fatigue crack initiation (formation plus small crack growth to some predefined size) for laboratory specimens, i.e.,

$$\frac{\Delta\varepsilon_p}{2} = \varepsilon_f'(2N_f)^c \tag{1}$$

where ε_f' is the fatigue ductility coefficient and c is the fatigue ductility exponent (ASTM Standard E606-00, 2000).

Two-parameter approaches have been developed as a multiaxial generalization of plastic strain amplitude in an extension of Eq. (1). Critical plane plastic strain range-based approaches have been introduced that consider cyclic plastic shear strain as the primary driving force for fatigue crack formation and early growth, with a modifying influence of normal stress or strain acting on the plane of maximum reversed plastic shear strain. In the present work we regard such quantities as fatigue indicator parameters (FIPs) in view of their relation to probability of crack formation and early growth. Fatemi and Socie (1988) and Fatemi and Kurath (1988) proposed a parameter for shear-dominated crack initiation that accounts for the observation that fatigue cracks initiate on planes of maximum shear for multiaxial loading conditions, i.e.,

$$P_{FS} = \frac{\Delta\gamma^p_{\max}}{2}\left(1 + k\frac{\sigma^n_{\max}}{\sigma_y}\right) \tag{2}$$

where $\Delta\gamma^p_{\max}$ is the maximum range of plastic shear strain and $\sigma^n_{\max}$ is the maximum normal stress acting on this plane. The stress, $\sigma^n_{\max}$, accounts for the effect of normal stress to the plane of small crack formation and growth, and is weighted by the material constant k. This term is normalized by the yield strength. Larger magnitudes of P_{FS} indicate a higher driving force for fatigue damage. The Fatemi–Socie (FS) parameter has been used to correlate fatigue damage formation over a large number of grains for a range of multiaxial loading conditions for materials with extended Stage I dominant regions such as 1045 steel and IN718 (McDowell and Berard, 1992; Socie, 1993).

Although the Fatemi–Socie FIP was originally only applied at the scale of laboratory specimens, several workers have applied this and similar FIPs at the microscale using crystal plasticity simulations. For example, Bennett and McDowell (1999) correlated microslip and mixed-mode behavior of microstructurally small crack growth to the Fatemi–Socie FIP and considered its distribution over the grains; moreover, the Fatemi–Socie FIP distributes heterogeneously over the grains. Moreover, they also observed that the Fatemi–Socie FIP correlates well with distributions of small fatigue cracks within the grains. Bennett and McDowell (2003) also used the Fatemi–Socie FIP to explore local grain orientation distribution effects on microslip in HCF. Other workers (Döring et al., 2006; Hoffmeyer et al., 2006) observed good agreement between the locally applied Fatemi–Socie FIP (determined using crystal plasticity calculations) and microstructurally small crack growth within the first few grains based on experiments in structural steel S460N. Dunne et al. (2006, 2007) used detailed simulations coupled with experiments to show that crystal plasticity can correlate precisely to localized plastic slip (and subsequent fatigue crack formation) in realistic Ni-base superalloy and Ti alloy microstructures. Findley and Saxena (2006) used the Fatemi–Socie FIP to examine the effect microstructure attributes such as grain size have on the local driving forces for fatigue damage formation. Zhang et al. (2009) and Prasannavenkatesan et al. (2009) also used the Fatemi–Socie FIPs to look at the local processes of fatigue crack formation at primary inclusions in carburized and shot-peened martensitic steel. We also point out that crystal plasticity models developed by Zhang and Jiang (2008) for pure polycrystalline Cu and by Bridier et al. (2009) for duplex Ti–6Al–4V have been successful at capturing localized plastic slip in these material systems. Such work demonstrates the ability of locally applied FIPs determined via crystal plasticity simulations to correlate microstructure scale slip with fatigue crack formation and early stages of microstructurally small crack growth for a range of ductile metallic polycrystalline material systems. In essence, there is similitude in scaling the relations between P_{FS} and the number of cycles to form and growth a fatigue crack to different length scales within the range of several microns to several hundred microns.

As discussed by McDowell (1996), these types of critical plane approaches for shear-dominated microcracking are related to Stage I shear-dominated propagation of MSCs with an influence of the normal stress to the slip/crack plane. Early work by Hoshide and Socie (1987) considered the affect of microplastic strain on fatigue damage formation and MSC crack growth under mixed-mode (I–II) loading. They correlated ΔJ from EPFM via a Paris type law with fatigue crack growth behavior

of small cracks. Moreover, Hoshide and Socie (1987) related ΔJ to the ranges of crack opening displacement (COD) and/or crack sliding displacement (CSD) for mode I and mode II, respectively. Later, McDowell and Berard (1992) employed ΔJ and argued for similarity of ΔCTD with the Fatemi–Socie parameter.

3. Results

3.1. Mesh quality study

As seen in Fig. 3, we impose a voxellated mesh to model the generated microstructures. A detailed study was performed to investigate the sensitivity of the convergence of the Fatemi–Socie FIP to these types of voxellated meshes. The parameters for the microstructures that were generated using the Voronoi based microstructure generator are given in Table 3. Four different microstructures were generated using the Voronoi based microstructure generator for this mesh study and are hereafter referred to as microstructures A, B, C and D. Two of the meshes with different numbers of elements for Microstructure C are shown in Fig. 5 with contours of accumulated plastic strain after three cycles. In each case, the elements belonging to the grain with the extreme value grain averaged Fatemi–Socie parameter of highest magnitude among all of the grains in the volume is highlighted in red. In the case of Microstructure C as seen in Fig. 5, the grain highlighted in red is contained entirely in the interior of the volume (i.e., the grain does not intersect the boundary) except for one element on the x–y surface. A description of the different meshes considered is given in Table 4. For the simulations, periodicity was imposed in all directions. The simulations were cycled in strain control with a maximum strain of 0.5% under completely reversed loading (i.e., $R = -1$). The distribution of the grain volume normalized by the target average grain volume of 1.0×10^{-6} mm^3 was fit to a log–normal distribution with the mean and standard deviation of the natural logarithm of the normalized grain volume given by -14.0 and 0.7, respectively. A strain rate of 0.002 s^{-1} was employed in these simulations. All calculations were performed over the entire volume.

The convergence of the extreme value Fatemi–Socie FIP as calculated over a single element and over all the elements of each grain is given in Fig. 6. In Fig. 6(a), we can see that the magnitude of the extreme value Fatemi–Socie FIP changes by as much at 20% across the meshes with 20–28 elements along an edge and convergence is not achieved. However, with grain size averaging volumes, variation in the extreme value FIP reduces to less than 5% in most cases across meshes with 14–28 elements along an edge. The grain with the observed extreme value FIP did not change when there were 12 or more elements along an edge or when the ratio of the element volume to average grain volume was greater than or equal to 0.064.

3.2. Statistical volume elements and size for IN100

As mentioned previously, we define our SVEs such that the local plastic response on the scale of the grains is unaffected by further increasing the volume of the SVE. Additionally, we require that the overall effective (i.e., macroscopic) elastic/plastic response is nearly the same for each SVE. To quantify the influence of SVE size on the FIPs we simulated several SVEs of different size. Specifically, we constructed several instantiations of cuboidal arrays of randomly oriented grains. These cuboidal grain arrays consist of blocks with 3, 5, 7, and 9 grains, respectively, along each edge with random periodic boundary conditions applied in all directions. In this manner the center grain has 1, 2, 3, and 4 neighbors, respectively, in each direction between itself and the applied periodic boundary conditions. In these simulations, these SVEs were cycled one time under completely reversed loading (i.e., $R = -1$) with a maximum strain magnitude of 1.0%. The quasistatic strain rate of 0.004 s^{-1} was used in these simulations. The grains were dimensioned 9 μm along each edge and consist of a total of 27 quadrilateral elements with reduced integration (type C3D8R in ABAQUS) or 3 elements along each edge. The orientation of the individual grains was random except for the center grain which was oriented in the $\langle 0\,0\,1\rangle$, $\langle 2\,1\,25\rangle$, and $\langle 1\,1\,1\rangle$ directions, respectively. We can see in Fig. 8 that crystals oriented near the $\langle 2\,1\,25\rangle$ and $\langle 1\,1\,1\rangle$ directions exhibit the maximum apparent Schmid factors for octahedral and cube slip, respectively. The Fatemi–Socie FIP averaged over the differently oriented center grains for the differently sized SVEs are given in Fig. 7. In all cases, there is a significant change in the grain averaged FIP of the center grain when the SVE is increased from 3 to 5 grains along each edge. However, as the number of grains along each edge are increased further from 5 to 7 or 7 to 9 further changes grain averaged FIP of the center grain are much less. Thus, for the purposes of this work, we assume that the primary zone of influence includes the two nearest neighbors of any one grain and that grains further out than that have much less influence. The SVEs for our microstructures for the subsequent study are scaled accordingly.

Table 3
Model parameters used for all simulated microstructure in the mesh quality study.

Edge length of microstructure volume	40 μm
Average cube root grain size	10 μm
Number of grains	77
Ratio of minimum spacing of grain centers to average distance between grain centers	0.3

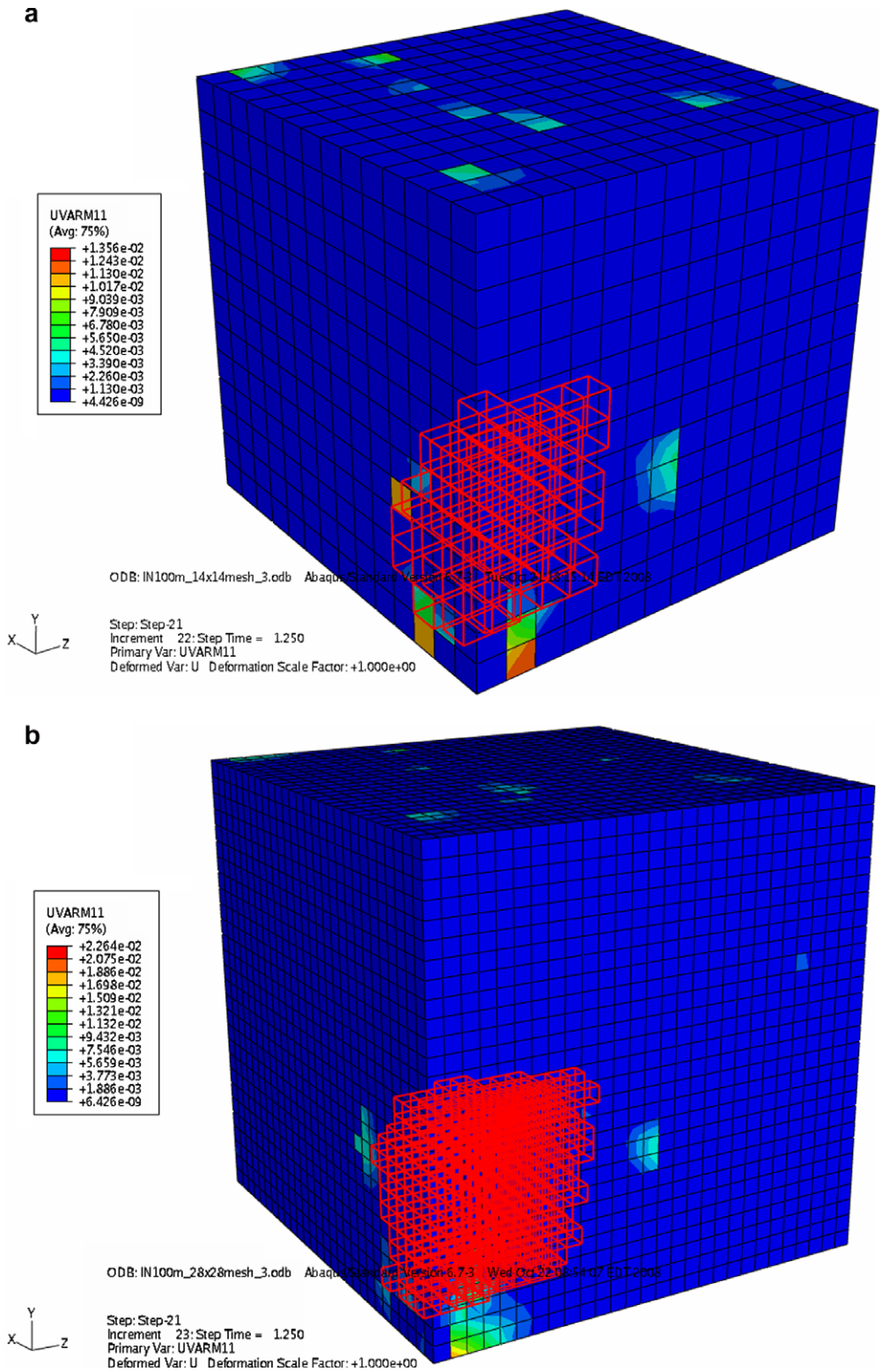

Fig. 5. The mesh and contours of accumulated plastic strain after three cycles at 0.5% strain with $R = -1$ for the 77 grain model for Microstructure C with (a) 14 and (b) 28 elements along each edge. The elements belonging to the grain with the extreme value FIP are highlighted in red. (For interpretation of the references to color in this figure legend, the reader is referred to the web version of this article.)

Table 4
Description of the different meshes considered in the mesh study for Microstructure A.

Number of elements along edge	Total elements	Element volume (mm^3)	Ratio of element volume to average grain volume
8	512	1.25×10^{-7}	0.1250
10	1000	6.40×10^{-8}	0.0640
12	1728	3.70×10^{-8}	0.0370
14	2744	2.33×10^{-8}	0.0233
16	4096	1.56×10^{-8}	0.0156
18	5832	1.10×10^{-8}	0.0110
20	8000	8.00×10^{-9}	0.0080
22	10,648	6.01×10^{-9}	0.0060
24	13,824	4.63×10^{-9}	0.0046
26	17,576	3.64×10^{-9}	0.0036
28	21,952	2.92×10^{-9}	0.0029

3.3. Extreme value fatigue response and microstructure in IN100

To investigate the influence of grain orientation, disorientation and grain size on IN100, multiple SVEs have been constructed using the Voronoi tessellation based microstructure generator and simulated via FEM, as previously described. Multiple SVEs for the local plastic response were generated and strained uniaxially at 0.3%, 0.5%, and 0.7% strain at a quasistatic strain rate of $\sim$0.002 s^{-1}. The macroscopic yield is observed for this particular IN100 at approximately near 1.0% strain. The

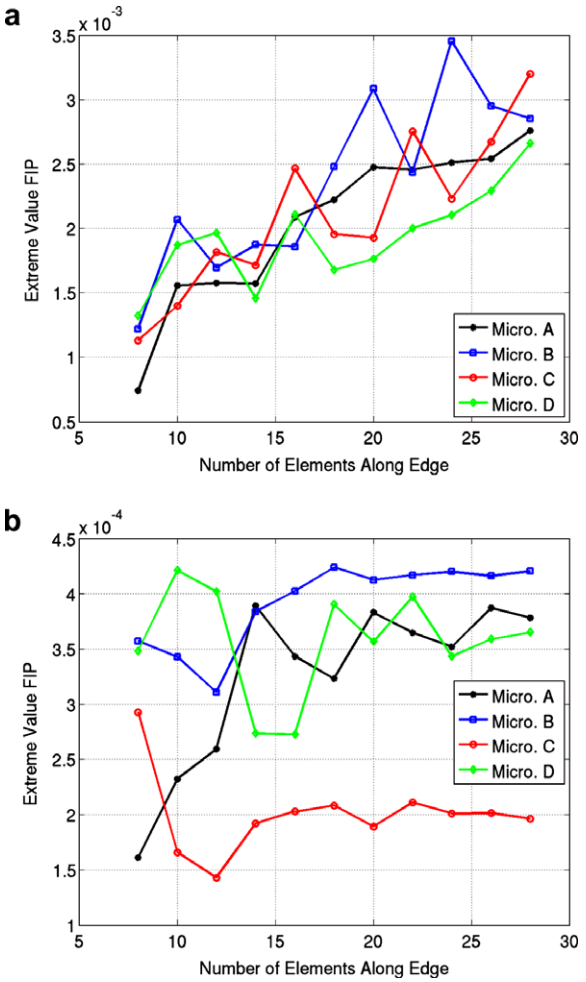

Fig. 6. Convergence of the extreme value Fatemi–Socie FIP for (a) the FIP calculated over a single element and (b) the FIP calculated over all the elements in a single grain. Although convergence was not achieved over the element sized averaging volume, variation was minimal over most of the meshes simulated for grain sized averaging volumes.

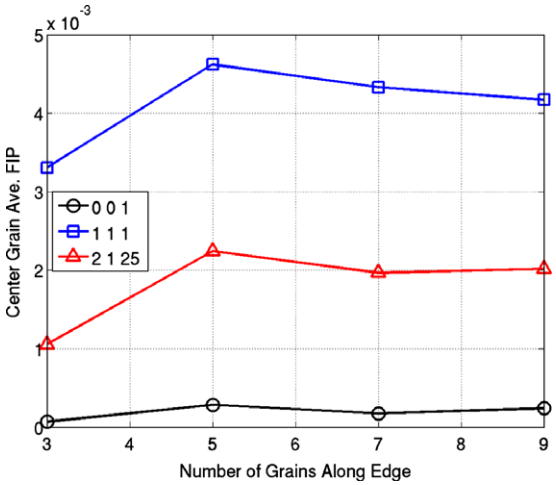

Fig. 7. Comparison of the grain averaged Fatemi–Socie FIP of the center grain oriented with its {0 0 1}, {1 1 1} and {2 1 25} planes perpendicular to the loading directions, respectively, versus the number grains along the edge of the SVE. These SVEs consisted of arrays of cuboidal grains each grain dimensioned 9 μm along an edge.

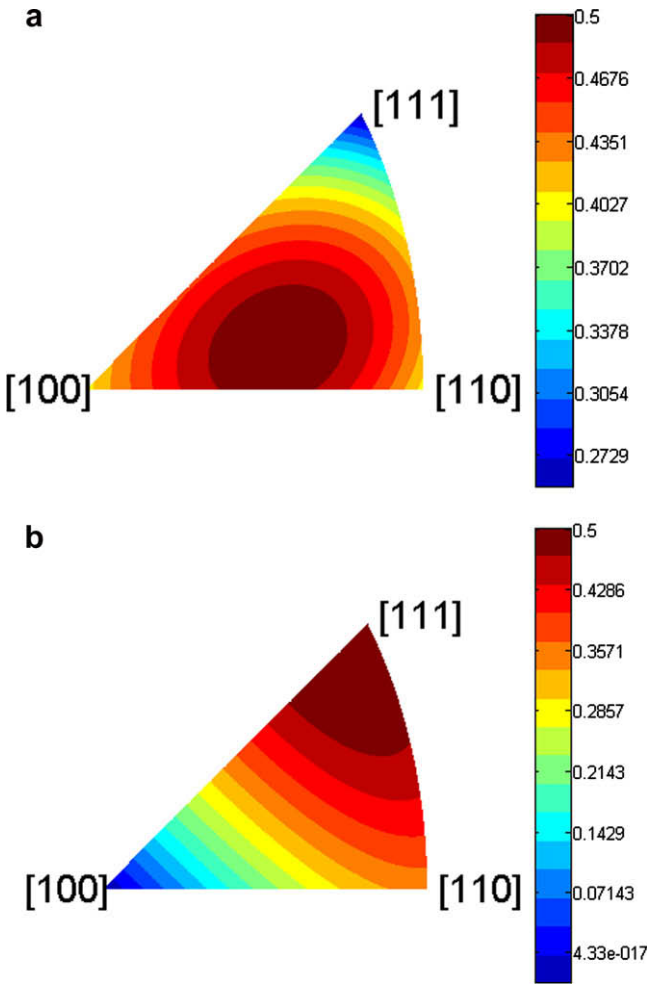

Fig. 8. Apparent Schmid factors based on crystallographic orientation for the (a) octahedral and (b) cube slip systems.

cyclic strains were completely reversed (i.e., $R = -1$). Each simulation was cycled three times to allow for an initial shakedown period before the results were analyzed. Periodic boundary conditions were applied in all directions. As in the previously described mesh study and SVE size study, the voxellated meshes of these generated microstructures consist of quadrilateral elements with reduced integration (type C3D8R in ABAQUS). The number of grains in the simulations was allowed to vary to best fit the imposed grain size distribution and ranged between 325 and 375 grains. Each SVE was dimensioned to 0.150 mm along each edge. The distribution of grain volumes normalized by the target average grain volume of 8.0×10^{-6} mm^3 was fit to a log–normal distribution with a mean of -12 and standard deviation of 0.4. This corresponds to a target average cube root grain size of $\sim$0.020 mm. There are 24 elements along each edge of the SVE or 13824 elements in all. The ratio of the element volume to the average target grain volume is 0.030. We simulated a total of 50 SVEs cycled at 0.3% strain, 100 SVEs cycled at 0.5%, and 50 SVEs cycled 0.7% strain.

It is of interest to now consider the exact character of the extreme value distributions of the Fatemi–Socie FIP as estimated from the simulated SVEs. To do this, we first give some brief background concerning extreme value statistical theory. Assuming that X is a random variable that is associated with a known cumulative distribution function $F_X(x)$, the maximum extreme value of a sample from X of size n can be defined as

$$Y_n = \max(X_1, X_2, \ldots, X_n). \tag{3}$$

If we require that Y_n is less than some value y, than all the random variables in the same sample associated with Y_n must also be less than y. The distribution function of Y_n is defined as the probability that for a sample of size n, Y_n is less than or equal to y, i.e.,

$$F_{Y_n}(y) \equiv P(Y_n \leq y) = P(X_1 \leq y, X_2 \leq y, \ldots, X_n \leq y). \tag{4}$$

If we assume that $X_1, X_2, \ldots, X_n$ are statistically independent and identically distributed, i.e.,

$$F_{X_1}(x) = F_{X_2}(x) = \cdots = F_{X_n}(x) = F_X(x), \tag{5}$$

the distribution function F_{Y_n} is related to F_X according to

$$F_{Y_n}(y) = [F_X(y)]^n. \tag{6}$$

Extreme value distributions for the minima can similarly be constructed. As the sample size n becomes large, the distribution described by Eq. (6) above has been observed in some cases to converge to certain limiting distributions or asymptotic distributions. For distributions of a single variable, it has been proven that there are only three types of non-degenerated distributions to which the extreme value distributions can converge for large n (Castillo, 1988; Galambos, 1978). The three possible non-degenerated asymptotic distributions for the maximum extreme value distributions can be expressed as (i) Frechet type, (ii) Weibull type, or (iii) Gumbel type. There are similar forms of these asymptotic distributions to which the minimum extreme value distributions can converge. The goal is to be able to characterize a dataset as belonging to one of these three types of distributions so that we can use the mathematical properties of these distributions to better understand the data.

Here we will show that the extreme value Fatemi–Socie parameters sampled from the simulated SVEs are well characterized by the asymptotic form of the extreme value Gumbel distribution, i.e.,

$$F_{Y_n}(y_n) = \exp[-e^{-\alpha_n(y_n - u_n)}] \tag{7}$$

where u_n is the characteristic largest value of the initial variable X, and α_n is an inverse measure of dispersion of the largest value of X. As noted previously, n refers to the size of the samples of the initial variable X in the set of distributions of X from which Y_n is sampled which for the asymptotic form is assumed to be very large. To visualize these extreme value distributions, we plot the extreme value FIPs for each SVE on a probability plot that has been linearized for the extreme value Gumbel distribution. This is demonstrated in Fig. 9, where we plot the extreme value Fatemi–Socie FIPs for sample sizes of 25, 50, 75, and 100 SVEs that have all been cycled at 0.5% strain. Here the extreme value Fatemi–Socie FIPs are estimated over grain sized volumes. In this plot, we note the probability p is linearized for the extreme value Gumbel distribution by $\ln(1/\ln(1/p))$ as seen on the vertical axes. The range of observed extreme values is then given by the abscissa. By scaling the axes in this manner, a true extreme value Gumbel distribution appears as a straight line. This linearization procedure and the method used to fit the experimental data to the extreme value Gumbel distribution is outlined in Appendix B. The fits for these sampled distributions to the Gumbel distribution appear in each case in Fig. 9 as lines. As can be seen in Table 5, these data are fit by the Gumbel distribution with high confidence (i.e., $R^2 > 0.97$), even for a sample size of just 25 simulated SVEs; moreover, the fitting parameters do not change significantly with increased sample sizes.

Fig. 10 shows the distributions of the extreme value Fatemi–Socie FIPs for the different strain magnitudes tested, 0.3%, 0.5%, and 0.7%. Again this plot is linearized for the Gumbel distribution as outlined in Appendix B. Additionally, in the extreme values of the FIPs are plotted in Fig. 10 on a log scale in order compare the distributions for the different strain magnitudes on the same plot. The parameters for fit of the Gumbel distributions to these observations are given in Table 6. We note that as the strain magnitude increases, the extreme value distributions of the Fatemi–Socie FIP tend to move to the right. This correlates with the fact that as the strain magnitude increases the driving forces for fatigue damage formation are higher. Thus, fatigue cracks form more rapidly and the portion of fatigue life attributed to fatigue crack formation is shorter.

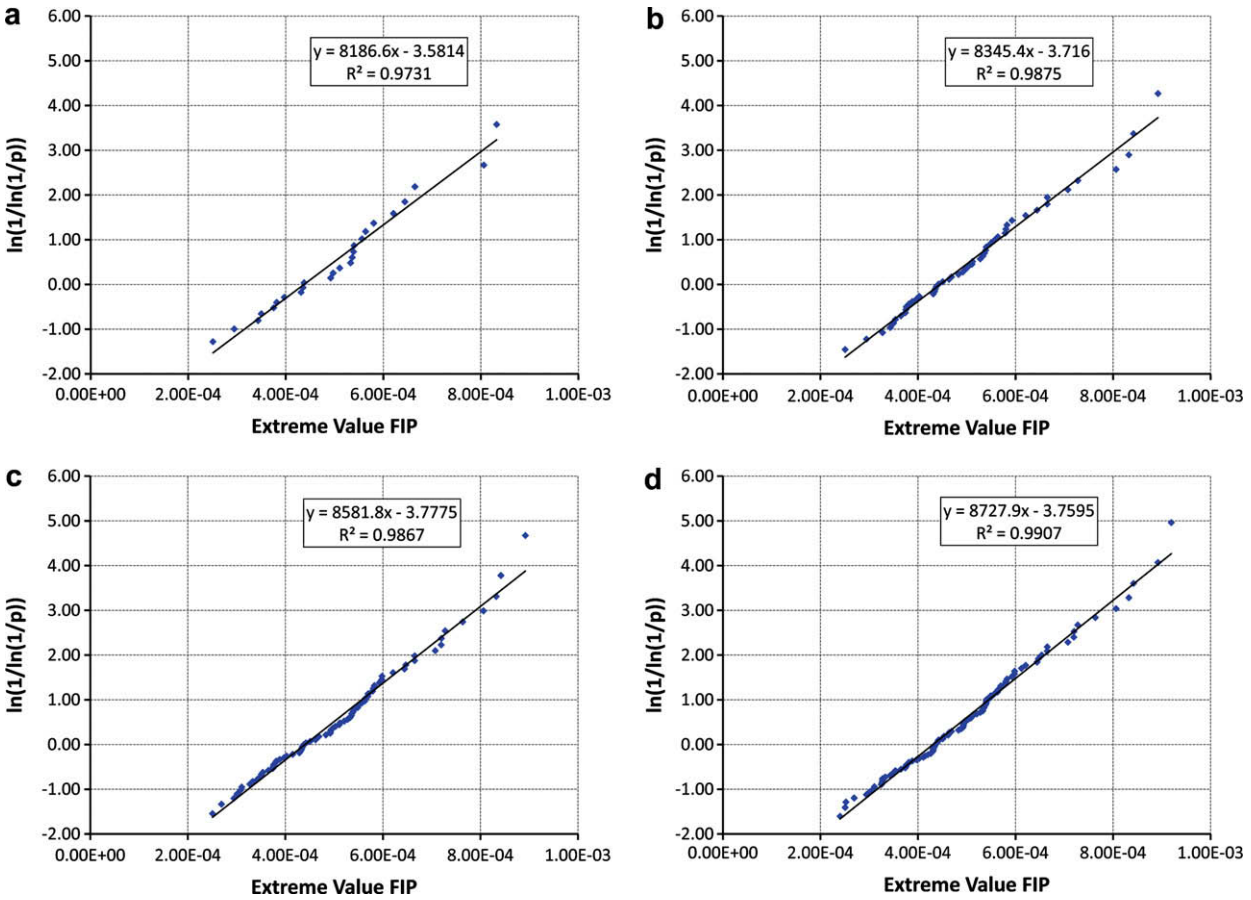

Fig. 9. Extreme value distribution of the Fatemi–Socie FIP as estimated over grain sized averaging volumes for (a) 25, (b) 50, (c) 75, and (d) 100 SVEs for the simulations cycled at 0.5% strain. The extreme value Fatemi–Socie FIP was selected to be the FIP with the highest magnitude out of all the FIP calculated over each grain.

Table 5
The parameters for the least squares fit of the Gumbel distribution (i.e., $F_{y_n}(y_n) = \exp[-e^{-\alpha_n(y_n-u_n)}]$) for the extreme value distributions of the Fatemi–Socie FIPs sampled over 25, 50, 75, and 100 SVEs, respectively, for 0.5% maximum strain. These extreme value distributions are plotted in Fig. 9. The goodness of fit is also given in terms of the R^2 value that ranges between 0 and 1 with 1 indicating a perfect fit.

#SVEs	α_n	u_n	R^2
25	8186.6	4.375E−04	0.973
50	8345.4	4.453E−04	0.988
75	8581.8	4.402E−04	0.987
100	8727.9	4.307E−04	0.991

Examination of the parameters for the Gumbel distribution fits of the estimated extreme value FIP distributions are informative in terms of the relative dispersion of the distributions for the different strain magnitudes. For the Gumbel distribution, α_n is an inverse measure of the dispersion of the largest values of the initial population (i.e., the parent distribution of the extreme value distribution) while u_n can be considered as the characteristic largest value of the initial population. Thus, the quantity $(\alpha_n)^{-1}/u_n$ is an indication of the dispersion of the extreme value distribution relative to the characteristic largest values of the initial population. In other words, larger values of $(\alpha_n)^{-1}/u_n$ indicate greater variation around the characteristic largest values than smaller values. In our case, as the strain magnitude increases the variation of the extreme value distributions of the distributions (i.e., $(\alpha_n)^{-1}/u_n$ from Table 6) tends to decrease. These data corroborate the *S–N* curve for IN100, as seen in Fig. 2(a) and (b) with the noted exception at 1150 MPa where there are arguably two competing modes of failure. As the stress/strain magnitude increases the overall variation in the fatigue lives decrease. Our results similarly show that variation of fatigue life associated with crack formation decreases as the magnitude of applied cyclic straining increases.

To understand how local attributes of microstructure influence the extreme value fatigue response as estimated via the FIPs, we consider the microstructure attributes in the neighborhoods where the extreme value FIPs were recorded. Here we

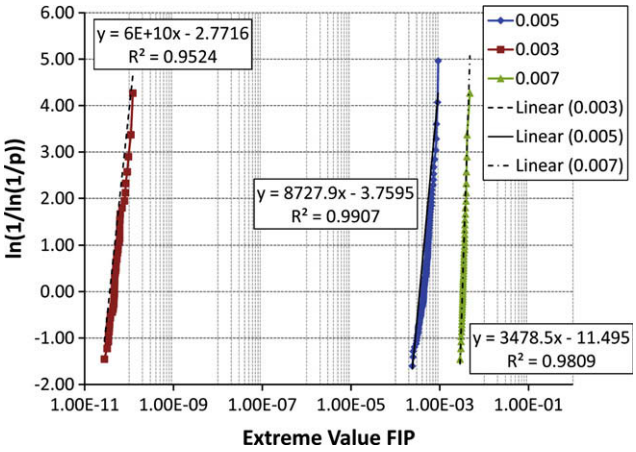

Fig. 10. The extreme value distribution of the Fatemi–Socie FIP as estimated over a single element and over the entire grain for the simulations cycled at 0.3%, 0.5%, and 0.7% strain. The extreme value Fatemi–Socie FIP was selected to be the FIP with the highest magnitude out of all the FIP calculated over each element or over each grain in each SVE.

consider two forms of the Schmid factor. The *apparent* Schmid factor for orientation g, m_a^g, is based purely on geometry, i.e., $m_a^g = \max\{\cos(\phi^i)\cos(\lambda^i),\ i = 1 \ldots n\}$, where ϕ^i is the angle between the ith slip plane normal and loading direction and λ^i is the angle between the ith slip direction and the direction of uniaxial applied stress on the SVE. The total number of slip systems is n. The *local* Schmid factor calculated over a volume ω, m_l^ω, is computed as the ratio between the maximum resolved shear stress (as estimated from the FE simulations) divided by the global SVE uniaxial applied stress, i.e., $m_l^\omega = \max(\tau_{rss}^i)/\sigma$ for $i = 1, \ldots, n$. In contrast to the apparent Schmid factor, the local Schmid factor considers the local stress state as affected by intergranular interactions and microplasticity. Thus, although the apparent Schmid factor is typically bounded between 0.27 and 0.5 for $\langle 1\ 1\ 0\rangle\{1\ 1\ 1\}$ octahedral slip, this is not the case for the local Schmid factor. In reality the local Schmid factor will be observed to be more broadly distributed between 0 and 1 due to load shedding or load shielding from neighboring grains, which affects the local stress fields in individual grains relative to the macroscopic applied loading conditions. For the calculations given below, the volumes over which we calculate the local Schmid factor correspond to the same volumes over which we calculate the FIPs. In contrast, the apparent Schmid factor is based on the orientation and relative loading direction at a single location (i.e., for a particular element) or for a grain.

First, we focus directly on the zones where the extreme value FIPs has been identified. In Fig. 11, we plot the extreme value Fatemi–Socie FIP as estimated over the volume of a single element versus the corresponding local Schmid factor for both the octahedral and cube slip systems for the applied maximum strain magnitudes of 0.3%, 0.5%, and 0.7%, respectively. Thus, in Fig. 11 each extreme value Fatemi–Socie FIP is associated with two Schmid factors, one for octahedral slip and one for cube slip. It is noted that as the maximum cyclic strain amplitude increases, the local Schmid factors associated with the extreme value FIPs tend to decrease slightly. This is logical because even though the far field stress may be increasing the flow stress will not change significantly. Therefore, the local Schmid factor will decrease in magnitude as the far field load increases. Secondly, we point out that in all cases the Schmid factors for cube slip are of greater magnitude than the local Schmid factors for octahedral slip as seen in Fig. 11. In other words, the grains in which the extreme value FIPs are identified all appear to be unfavorably oriented for octahedral slip.

We also consider certain correlated microstructure attributes at the locations of the FIPs as the second part of the microstructure-sensitive extreme value statistical framework. As discussed previously, the primary microstructure attribute considered in this study is crystallographic orientation. We construct the extreme value marked radial correlation function for the apparent Schmid Factor (i.e., $R^{\max(\alpha)}(m_a^g, m_a^{g'}|r, \Omega)$). By using the apparent Schmid factor, we really are indirectly quantifying the probabilities of specific grain orientations and misorientations existing coincident with the observed extreme value FIPs. As will be seen later, constructing the extreme value correlation function with the apparent Schmid factor instead of the more direct microstructure attribute of crystalline orientation simplifies the interpretation of the results. We choose not to

Table 6
The parameters for the least squares fit of the Gumbel distribution (i.e., $F_{Y_n}(y_n) = \exp[-e^{-\alpha_n(y_n-u_n)}]$) for the extreme value distributions of the Fatemi–Socie FIP for the different maximum strain levels simulated. The goodness of fit is also given in terms of the R^2 value that ranges between 0 and 1, with 1 indicating a perfect fit.

% strain	α_n	u_n	$(\alpha_n)^{-1}/u_n$	R^2
0.30	6.0×10^{10}	4.619×10^{-11}	0.361	0.952
0.50	8727.9	4.307×10^{-4}	0.266	0.991
0.70	3478.5	3.305×10^{-3}	0.087	0.981

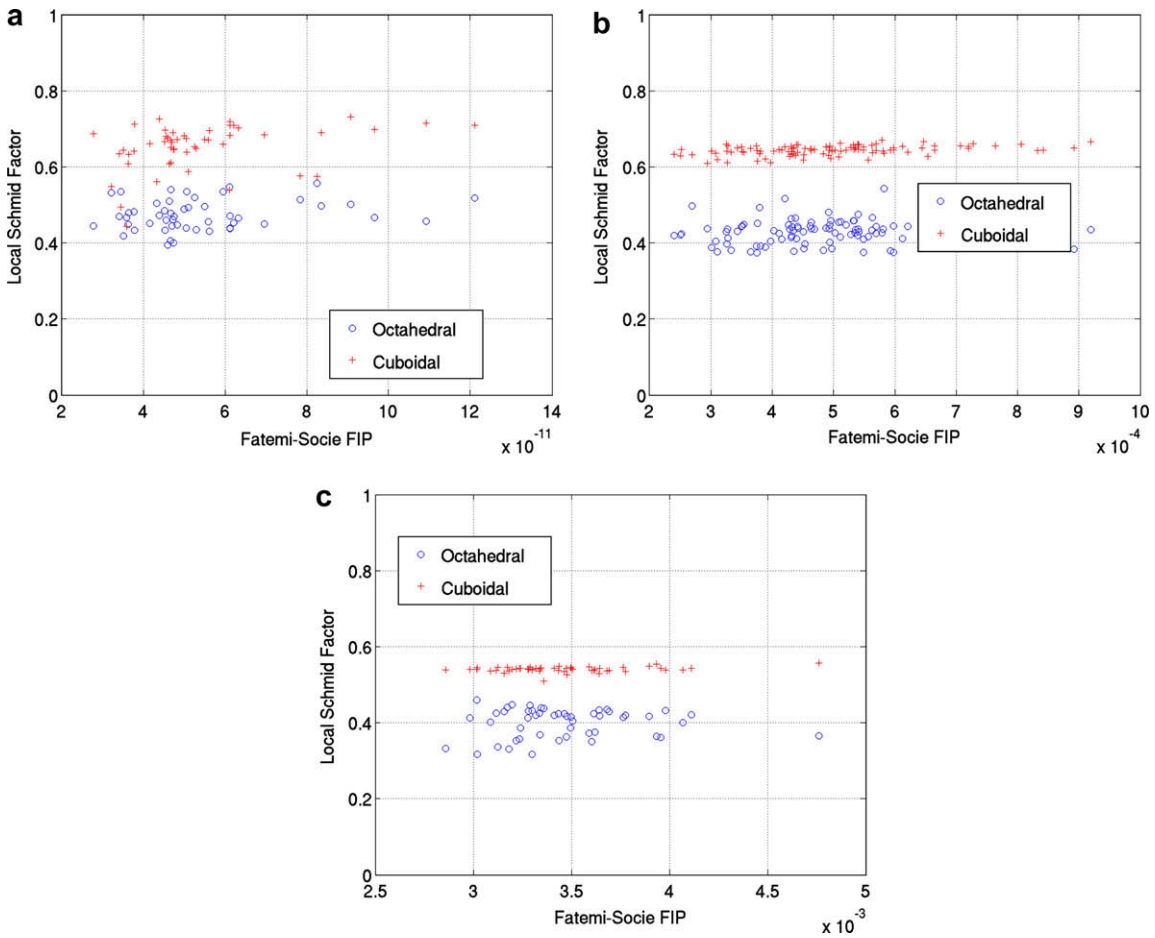

Fig. 11. Scatter plot of the extreme value Fatemi–Socie FIP (abscissa) versus the local Schmid factor (ordinate) for simulations over (a) 50 SVEs at 0.3% strain, (b) 100 SVEs at 0.5% strain, and (c) 50 SVEs at 0.7% strain.

use the local Schmid factor computed using the pointwise stress tensor acting on slip systems at each point in the mesh because the local Schmid factor is more of a response parameter than a direct description of the local microstructure attribute of interest (i.e., grain orientation).

In Fig. 12, we plot the complete radial distribution estimated over the entire ensemble of simulated SVEs and the extreme value marked distribution functions sampled only at the location of the extreme value FIPs for the 100 SVEs cycled at 0.5% strain. The particular correlations plotted here for the local Schmid factors for $m_a^g = 0.45—0.5$ (for cube slip) and $m_a^{g'} = 0.45—0.5$ (for cube slip) in Fig. 12(a) and complete radial and extreme value marked radial distribution of Schmid factors $m_a^g = 0.45—0.5$ (for cube slip) and $m_a^{g'} = 0.45—0.5$ (for octahedral slip) in Fig. 12(b) were selected because they occurred with the highest probability at the extreme value location of the FIPs. In Fig. 12(a), we look at the auto-correlations between Schmid Factors $m_a^g = 0.45—0.5$ (for cube slip). We see that below one average grain size, the probability of finding $m_a^g = 0.45—0.5$ (for cube slip) at the location of the extreme value response is as high as 33%; in contrast, the probability of finding this particular orientation in the *complete* microstructure ensemble is only 20%. Similarly, the probability of finding $m_a^g = 0.45—0.5$ (for cube slip) near $m_a^{g'} = 0.45—0.5$ (for octahedral slip) (as can be seen in Fig. 12(b)) is as high as 0.47 at a distance of one average grain size; whereas, the probability of these correlated orientation existing in the complete microstructure ensemble is less than 0.2. In essence, we observe a high probability of finding a high FIPs in a region with clusters of grains oriented for cube slip or clusters of grains oriented for cube slip surrounded by soft grains oriented for easy octahedral slip.

With an understanding of how the slip planes are oriented relative to the loading direction as described by the apparent Schmid factor, it is also interesting to explore the distributions of the local Schmid factors in the regions identified to be critical by the extreme value FIPs. In Fig. 13, we plot the probability density of the local Schmid factors m_l for all the grains and for the grains with the apparent Schmid factors $m_a = 0.45$ to $m_a = 0.5$ for both the octahedral and cube slip systems, respectively. When we consider the distribution of the local Schmid factor over all of the grains we notice that the maximum local Schmid factors for octahedral slip are less than the maximum local Schmid factors for cube slip. This suggests that the resolved shear stresses on the cube slip systems can be much larger than they are on the octahedral slip systems. As

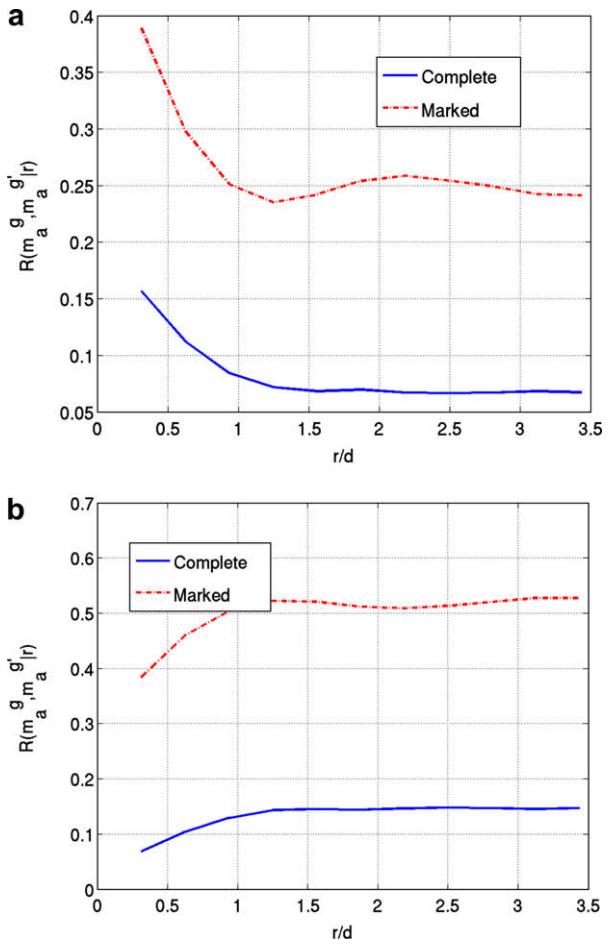

Fig. 12. For IN100 the (a) complete radial and extreme value marked radial distribution for apparent Schmid factors $m_a^{g\prime} = 0.45{-}0.5$ (cube slip) and $m_a^{g\prime} = 0.45{-}0.5$ (cube slip) and (b) complete radial and extreme value marked radial distribution of apparent Schmid factors $m_a^{g\prime} = 0.45{-}0.5$ (cube slip) and $m_a^{g\prime} = 0.45{-}0.5$ (octahedral slip) are plotted for the 100 SVEs subjected to 0.5% strain. The distance r that separates the two orientations is normalized against the average cube root grain size d (i.e., 20 μm).

expected, when the apparent Schmid factor is larger (i.e., between 0.45 and 0.5) for cube slip, the corresponding local Schmid factors are much more likely to be larger than the local Schmid factors for cube slip. It is interesting to note, however, that for larger Schmid factors for octahedral slip (i.e., 0.45–0.5) we observe that the local Schmid factor for cube slip can be larger than the local Schmid factor for octahedral slip. Thus, in some cases even when the Schmid factors for octahedral slip are high, the actual resolved stresses can be larger on some of the cube slip planes than on the octahedral slip planes.

4. Discussion

The extreme value distributions of the Fatemi–Socie FIP are well fit by the extreme value Gumbel distribution (i.e., $R^2 > 0.97$) in the Ni-base superalloy, IN100, in HCF. This observation is evident with as few as 25 simulation points as seen in Fig. 9. We hypothesize that the distributions of the extreme value Fatemi–Socie parameter is directly related to distributions of crystallographic fatigue damage formation in this and similar material systems. Thus, assuming an averaging volume for the relevant FIP that corresponds to crack incubation at this scale, one may postulate a relation such as $P_{FS} = \tilde{\gamma}_f'(2N_{inc})^c$, where $\tilde{\gamma}_f'$ is a fatigue ductility coefficient appropriate to crack formation at the scale considered. This is obviously related to the form of the Coffin–Manson law as defined in Eq. (1), with rescaling of parameter $\tilde{\gamma}_f'$ to correspond to a crack size on the order of microstructure. Using this type of relation, optimization problems can be envisioned regarding polycrystalline orientation distributions to achieve target HCF lives or variability thereof.

This work has considered only crystallographic fatigue damage formation and did not account for the effect of voids or non-metallic inclusions relative to their influence on the local driving forces for fatigue damage formation. Indeed, in IN100 the role of non-metallic inclusions is very important in forming life-limiting fatigue cracks. Each of these attributes can have an effect on overall variability of fatigue damage formation in this material system and must be considered for

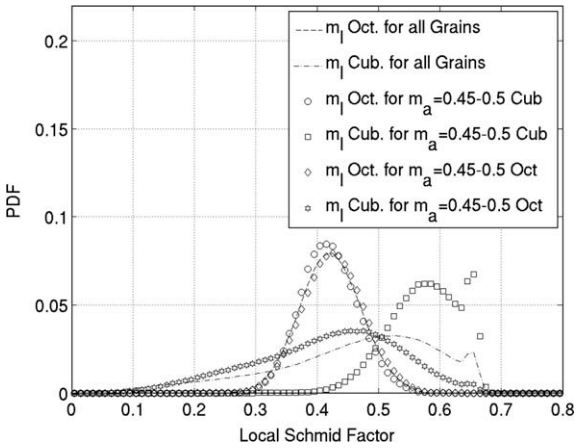

Fig. 13. Probability density of the local Schmid factors m_l for the octahedral and cube slip systems for all grains and for the grains with the apparent Schmid factors $m_a = 0.45$ to $m_a = 0.5$ for both the octahedral and cube slip systems, respectively.

any new material development. The understanding of extreme value slip behavior in this material system, however, is very important to the understanding of fatigue crack formation around inclusions/voids. For example, one can imagine a sample of IN100 with two inclusions of very similar character (i.e., phase, size, shape) where a fatigue crack forms at one of the inclusions and not the other when the material is subjected to some specified cyclic loading condition. Likely, an understanding of the local grain character (i.e., size, shape, orientation, misorientation) near the inclusion where the fatigue crack formed relative to the inclusion void of fatigue damage will be sufficient to explain the different responses in the neighborhood around the two inclusions.

Consideration of the extreme value marked radial distributions of the apparent Schmid factor allows us to readily observe the character of slip that is predicted to exist at the location of the extreme value response (i.e., FIPs). Here we observed that grains oriented unfavorably for octahedral slip or favorably for cube slip are predicted to exist with high probability at the locations of extreme value fatigue response in IN100. Moreover, clusters of grains oriented for cube slip or clusters of grains oriented for cube slip surrounded by grains oriented favorable for octahedral slip are predicted to exist with high probability at the location of the extreme value fatigue response. These simulations support the observations made in IN100 by Li et al. (2004) who observed fatigue damage formation along {1 0 0} planes in grains oriented unfavorable for octahedral slip. Thus, following our previous logic, we expect that clusters of grains oriented unfavorably for octahedral slip near inclusions or voids are more susceptible to fatigue crack formation than inclusions or voids that are not located in such clusters.

As improved next generation microstructure-sensitive constitutive models become available, they can serve the needs of the microstructure-sensitive statistical framework developed here. In fact, an interesting question is the extent of accuracy required of these models to deliver useful information for minimum life (low probability of failure) design of the microstructure against fatigue. It is an open issue.

5. Conclusions

The proposed statistical framework that captures the extreme value distributions of the FIP responses coupled with the extreme value marked correlation functions has allowed us to assess the distribution of driving force(s) for fatigue damage formation (i.e., crack nucleation and microstructurally small crack growth) in polycrystalline IN100. In these simulations, we account for the material microstructure, applied strain amplitude and strain state, and critically stressed volume of interest in HCF scenarios. Specifically, we found that:

- The extreme value distributions of the Fatemi–Socie fatigue indicator parameters (FIPs) that estimate the driving forces for fatigue damage formation appear are fit with high confidence (i.e., $R^2 > 0.97$) by the Gumbel distribution.
- The shape of the extreme value distributions of the Fatemi–Socie FIPs appears to be well defined with as few as 25 SVEs (i.e., microstructure instantiations) as demonstrated by the similarity in the parameters of the fits of the observations to the Gumbel distributions for sample sizes of 25, 50, 75, and 100 SVEs.
- These simulations predict that cube slip may play an important role in fatigue damage formation particularly when there are multiple grains oriented for cube slip clustered in the same region or clusters of grains oriented for cube slip surrounded by other grains oriented favorable for octahedral slip. These observations support the results of previous experiments of fatigue in this material system (Li et al., 2004). Thus, as fatigue crack formation is dominated by the presence of non-metallic inclusions or voids for this particular material system, we expect that given two inclusions of similar character that fatigue cracks will form preferentially near the inclusion that is surrounded by grains or grain clusters unfavorably oriented for octahedral slip.

Acknowledgments

The authors would like to acknowledge the support of the NSF Center for Computational Materials Design, a joint Penn State-Georgia Tech I/UCRC, for development of extreme value HCF and VHCF statistical methods informed by microstructure-sensitive computational models. In addition, Craig P. Przybyla is grateful for the financial support of the Graduate Coop Program at the Air Force Research Laboratory at Wright Patterson Air Force Base, Dayton, Ohio. We are very appreciative of the insight offered relative to fatigue damage formation in Ni-base superalloys offered by Dr. Sushant Jha, Dr. Kezhong Li, and Dr. Michael Caton of the Air Force Research Laboratory through our many discussions. We also thank Dr. Michael Uchic of the Air Force Research Laboratory for his valuable feedback concerning our initial simulation results. In addition, Dr. Thomas Cruse is gratefully acknowledged for his helpful guidance in fitting the extreme value distributions.

Appendix A. Equations and parameters of the microstructure-sensitive crystal plasticity model for IN100 at 650 °C

The equations for the of the microstructure-sensitive crystal plasticity model for IN100 at 650 °C are given in Table A1 and are explained in detail by Shenoy et al. (2007, 2008). For the subsolvus microstructure considered here, the sizes and volume fractions of γ' precipitates are given by $f_{p1} = 0.053$, $d_2 = 320 \times 10^{-6}$ mm, $f_{p2} = 0.439$, $d_3 = 17 \times 10^{-6}$ mm, $f_{p3} = 0.078$, and the mean grain size is $d_{gr} = 6.6 \times 10^{-3}$ mm. Initial values of all slip system back stresses are set to zero. Parameters of the microstructure-sensitive crystal plasticity model for this IN100 microstructure at 650 °C are listed in Table A2.

Table A1
Equations of the microstructure-sensitive crystal plasticity model for IN100 at 650 °C.

Flow rule with back stress, threshold stress and drag stress

$$\dot{\gamma}^{\alpha} = \left[\dot{\gamma}_1 \left\langle \frac{|\tau^{\alpha} - \chi^{\alpha}| - \kappa^{\alpha}_{\lambda}}{D^{\alpha}} \right\rangle^{n_1} + \dot{\gamma}_2 \left\langle \frac{|\tau^{\alpha} - \chi^{\alpha}|}{D^{\alpha}} \right\rangle^{n_2}\right] \mathrm{sgn}(\tau^{\alpha} - \chi^{\alpha}) \tag{A.1}$$

where D^{α} is the drag stress (constant). The threshold stress is given by

$$\kappa^{\alpha}_{\lambda} = \kappa^{\alpha}_{0,\lambda} + \alpha_t \tilde{\mu} \tilde{b} \sqrt{\rho^{\alpha}_{\lambda}} \quad \text{for } \lambda = oct,\ cub \tag{A.2}$$

where $\tilde{\mu} = (f_{p1} + f_{p2} + f_{p3})\mu_{\gamma'} + f_m \mu_m$ and $\tilde{b} = (f_{p1} + f_{p2} + f_{p3}) b_{\gamma'} + f_m b_{\gamma}$.
Also,

$$\begin{matrix} \kappa^{\alpha}_{0,oct}\left[(\tau^{\alpha}_{0,oct})^{n_k} + \psi_{oct}(f_{p1}, d_2, f_{p2}, d_3, f_{p3})^{n_k}\right]^{1/n_k} + (f_{p1} + f_{p2})\tau^{\alpha}_{ns} \\ \kappa^{\alpha}_{0,cub}\left[(\tau^{\alpha}_{0,oct})^{n_k} + \psi_{oct}(f_{p1}, d_2, f_{p2}, d_3, f_{p3})^{n_k}\right]^{1/n_k} \end{matrix} \tag{A.3}$$

where $\tau^{\alpha}_{ns} = h_{pe}\tau^{\alpha}_{pe} + h_{cb}|\tau^{\alpha}_{cb}| + h_{se}\tau^{\alpha}_{se}$ (non-Schmid term),

$$\psi_{oct} = \psi_{cub} = \left[c_{p1}\sqrt{\zeta \frac{f'_{p1}}{d_1}} + c_{p2}\sqrt{\zeta \frac{f'_{p2}}{d_2}} + c_{p3}\sqrt{\zeta f'_{p3} d_3} + \frac{c_{gr}}{\sqrt{d_{gr}}}\right], \quad \zeta = \frac{\Gamma_{APB}}{\Gamma_{APB\_ref}},$$

$$f'_{p1} = \frac{f_{p1}}{f_{p1} + f_m}, \quad f'_{p2} = \frac{f_{p2}}{f_{p2} + f_m}, \quad \text{and} \quad f'_{p3} = \frac{f_{p3}}{f_{p3} + f_m}.$$

Internal state variables
(a) Dislocation density

$$\dot{\rho}^{\alpha}_{\lambda} = h_0\{Z_0 + k_1\sqrt{\rho^{\alpha}_{\lambda}} - k_2\rho^{\alpha}_{\lambda}\}|\dot{\gamma}^{\alpha}| \quad \text{(self-hardening)} \tag{A.4}$$

where $Z_0 = \frac{k_s}{b d_{\delta eff}}$ and $d_{\delta eff} \approx \left(\frac{2}{d_{2s}}\right)^{-1}$.

(b) Back stress

$$\dot{\chi}^{\alpha}_{\lambda} = C_{\chi}\{\eta\tilde{\mu}\tilde{b}\sqrt{\rho^{\alpha}_{\lambda}}\mathrm{sgn}(\tau^{\alpha} - \chi^{\alpha}_{\lambda}) - \chi^{\alpha}_{\lambda}\}|\dot{\gamma}^{\alpha} \quad \text{(self-hardening)} \tag{A.5}$$

where $\eta = \frac{\eta_0 Z_0}{Z_0 + k_1\sqrt{\rho^{\alpha}_{\lambda}}}$.

Table A2
Parameters of the microstructure-sensitive crystal plasticity model for IN100 at 650 °C.

$\tau^{\alpha}_{o,oct}$ (MPa)	$\tau^{\alpha}_{o,cub}$ (MPa)	c_{p1}	c_{p2}	c_{p3}	c_{gr} (MPa $\sqrt{mm}$)	k_{δ}
85.1	170.2	1.351	1.351	1.22×10^5	9.432	2.5×10^{-3}

$b_{\gamma'}$ (nm)	b_{γ} (nm)	$\mu_{\gamma'}$ (MPa)	μ_{γ} (MPa) (=μ_m)	k_1 (mm^{-1})	k_2	D^{α} (MPa)	h_o
0.25	0.41	81,515	130,150	2.6×10^5	8.2	150 (oct), 180 (cub)	4.8 (oct), 2.4 (cub)

h_{pe}	h_{cb}	h_{se}	η_o	$\Gamma_{APB}(=\Gamma_{APB\_ref})$ (J/m^2)	$\dot{\gamma}_1$ (s^{-1})	$\dot{\gamma}_2$ (s^{-1})
0.8	0.0	−0.4	2.82	164×10^{-3}	8.7	3.9×10^{-11}

$C_{11\gamma'}$ (MPa)	$C_{12\gamma'}$ (MPa)	$C_{44\gamma'}$ (MPa)	$C_{11\gamma}$ (MPa)	$C_{12\gamma}$ (MPa)	$C_{44\gamma}$ (MPa)	n_{κ}
135,000	59,210	81,515	158,860	73,910	130,150	1

n_1	n_2	$\rho^{\alpha}_{s}(0)$ (mm^{-2})	α_t* (MPa)	C_{χ}* (MPa)
15	9	1.0×10^5	0.0385	2.713

* Specific values for this microstructure, with all other parameters independent of microstructure.

$$\text{Also, } \dot{\gamma}_1 = \dot{\gamma}_0 \exp\left(\frac{-Q_1}{RT}\right), \quad \dot{\gamma}_2 = \dot{\gamma}_0 \exp\left(\frac{-Q_2}{RT}\right), \quad \dot{\gamma}_0 = 6.1 \times 10^{16}\ s^{-1},$$

where T = 923 K (650 °C), R = 8.314 J/(mol-K) and Q_1 = 280,000 J/mol, Q_2 = 480,452 J/mol.

Appendix B. Linearization and fit of the Gumbel distribution

The cumulative distribution function (CDF) of the Gumbel (Gumbel, 1958; Castillo, 1988) (extreme value) distribution for the largest values Y_n can be expressed as

$$F_{Y_n}(y_n) = \exp\left[-e^{-\alpha_n(y_n-u_n)}\right] \tag{B.1}$$

where u_n is the characteristic largest value of the initial variable X, and α_n is an inverse measure of dispersion of the largest value of X. Here n refers to the size of the samples of the initial variable X in the set of distributions of X from which Y_n is sampled. The expression in Eq. (B.1) is the asymptotic form of the Type I extreme value distribution of the largest values and therefore is valid as the sample size n approaches infinity (Castillo, 1988).

To linearize the Gumbel distribution, we solve Eq. (B.1) for the estimated parameter y_n given a probability p, i.e.,

$$\ln\left[\ln\left(\frac{1}{p}\right)\right]^{-1} = \alpha_n y_n - \alpha_n u_n \tag{B.2}$$

Thus, we now have an expression in the form of $y = mx + b$ where $y = \ln[\ln(1/p)]^{-1}$, $m = \alpha_n$, $x = y_n$, and $b = -\alpha_n u_n$.

Ranking the data from a sample of the extreme value distribution Y_n in the order of smallest to largest (i.e., $y_n^1, y_n^2, \ldots, y_n^n$), one can determine estimators $F_{Y_n}(y_n^1)$, $F_{Y_n}(y_n^2)$, $F_{Y_n}(y_n^1)$, etc. using the median rank statistic defined as

$$\tilde{y} = \frac{j - 0.3}{n + 0.4} \tag{B.3}$$

for the jth ranked observation in a sample of size n (Kapur and Lamberson, 1977). Here the superscripts on y_n refer to their rank for a particular sample of Y_n. The procedure then to plot a given dataset on a linearized scale for the Gumbel distribution is:

1. Using Eq. (B.3), we estimate the probability p for each observation y_n in the dataset.
2. Determine $\ln[\ln(1/p)]^{-1}$ for each observation and plot it against the original observation.
3. Using a least squares fit, a line of the form $y = mx + b$ is fit to the data.
4. The estimated parameters for the distribution is determined according to $m = \alpha_n$, $x = y_n$, and $b = -\alpha_n u_n$.

This general procedure is outlined and explained in detail by Kapur and Lamberson (1977) for similar distributions.

References

ABAQUS, 2007. Version 6.7, third ed. Simulia, Providence, RI.
Antolovich, S.D., Jayaraman, N., 1983. Metallurgical instabilities during the high-temperature low-cycle fatigue of nickel-base super-alloys. Materials Science and Engineering 57, L9–L12.
ASTM Standard E606-00, Standard Test Method for Strain-Controlled Fatigue Testing, Annual Book of ASTM Standards, 2000. In: Annual Book of ASTM Standards, vol. 03.01. American Society for Testing and Materials, Philadelphia, PA, pp. 525–539.

Atkinson, H.V., Shi, G., 2003. Characterization of inclusions in clean steels: a review including the statistics of extremes methods. Progress in Materials Science 48, 457–520.
Aurenhammer, F., 1991. Voronoi diagrams: a survey of a fundamental geometric date structure. Computing Surveys 23, 345–405.
Barbe, F., Decker, L., Jeulin, D., Cailletaud, G., 2001a. Intergranular and intragranular behavior of polycrystalline aggregates. Part 1: F.E. model. International Journal of Plasticity 17, 513–536.
Barbe, F., Forest, S., Cailletaud, G., 2001b. Intergranular and intragranular behavior of polycrystalline aggregates. Part 2: Results. International Journal of Plasticity 17, 537–563.
Barber, C.B., Huhdanpaa, H., 2003. QHULL. The Geometry Center, Minneapolis, MN.
Bennett, V.P., McDowell, D.L., 1999. Polycrystal orientation effects on microslip and mixed-mode behavior of microstructurally small cracks. In: Miller, K.J., McDowell, D.L. (Eds.), Mixed-Mode Crack Behavior. American Society for Testing and Materials, West Conshohocken, PA, pp. 203–228.
Bennett, V.P., McDowell, D.L., 2003. Polycrystal orientation distribution effects on microslip in high cycle fatigue. International Journal of Fatigue 25, 27–39.
Bettge, D., Österle, W., 1999. "Cube slip" in near-[1 1 1] oriented specimens of a single-crystal nickel-base superalloy. Scripta Materialia 40, 389–395.
Bridier, F., McDowell, D.L., Villechaise, P., Mendez, J., 2009. Crystal plasticity modeling of slip activity in Ti–6Al–4V under high cycle fatigue loading. International Journal of Plasticity 25, 1066–1082.
Castillo, E., 1988. Extreme Value Theory in Engineering. Academic Press, Boston.
Coffin Jr., L.F., 1954. A study of the effects of cyclic thermal stresses on a ductile metal. Transactions of the American Society of Mechanical Engineers 76, 931–950.
Döring, R., Hoffmeyer, J., Seeger, T., Vormwald, M., 2006. Short fatigue crack growth under nonproportional multiaxial elastic–plastic strains. International Journal of Fatigue 28, 972–982.
Dunne, F.P.E., Wilkinson, A.J., Allen, R., 2006. Experimental and computational studies of low cycle fatigue crack nucleation in a polycrystal. International Journal of Plasticity 23, 273–295.
Dunne, F.P.E., Rugg, D., Walker, A., 2007. Length scale-dependent, elastically anisotropic, physically-based hcp crystal plasticity: application to cold-dwell fatigue in Ti alloys. International Journal of Plasticity 23, 1061–1083.
Fatemi, A., Kurath, P., 1988. Multiaxial fatigue life predictions under the influence of mean stress. Journal of Engineering Materials and Technology 110, 380–388.
Fatemi, A., Socie, D.F., 1988. A critical plane approach to multiaxial fatigue damage including out-of-phase loading. Fatigue & Fracture of Engineering Materials & Structures 11, 149–165.
Findley, K.O., Saxena, A., 2006. Low cycle fatigue in Rene 88DT at 650 degrees C: crack nucleation mechanisms and modeling. Metallurgical and Materials Transactions A: Physical Metallurgy and Materials Science 37A, 1469–1475.
Galambos, J., 1978. The Asymptotic Theory of Extreme Order Statistics. John Wiley & Sons, New York.
Goto, M., Knowles, D.M., 1998. Initiation and propagation behaviour of microcracks in Ni-base superalloy Udimet 720 Li. Engineering Fracture Mechanics 60, 1–18.
Gross, D., Li, M., 2002. Constructing microstructures of poly- and nanocrystalline materials for numerical modeling and simulation. Applied Physics Letters 80, 746–748.
Gumbel, E.J., 1958. Statistics of Extremes. Columbia University Press, New York.
Hoffmeyer, J., Döring, R., Seeger, T., Vormwald, M., 2006. Deformation behaviour, short crack growth and fatigue lives under multiaxial nonproportional loading. International Journal of Fatigue 28, 508–520.
Hoshide, T., Socie, D.F., 1987. Mechanics of mixed mode small fatigue crack growth. Engineering Fracture Mechanics 26, 841–850.
Hyzak, J.M., Bernstein, I.M., 1982. The effect of defects on the fatigue crack initiation process in 2 p/m super-alloys. 1: Fatigue origins. Metallurgical Transactions A: Physical Metallurgy and Materials Science 13, 33–43.
Jha, S.K., Caton, M.J., Larsen, J.M., Rosenberger, A.H., Li, K., Porter, W.J., 2005. Superimposing mechanisms and their effect on the variability in fatigue lives of a nickel-based superalloy. In: Larsen, J.M., Christodoulou, L., Calcaterra, J.R., Dent, M.L., Derriso, M.M., Hardman, W.J., Jones, J.W., Russ, S.M. (Eds.), Materials Damage Prognosis. TMS (The Minerals, Metals & Materials Society).
Jha, S.K., Caton, M.J., Larsen, J.M., 2007. A new paradigm of fatigue variability behavior and implications for life prediction. Materials Science and Engineering A: Structural Materials Properties Microstructure and Processing 468, 23–32.
Jha, S.K., Caton, M.J., Larsen, J. M., 2008. Mean vs. Life-Limiting Fatigue Behavior of a Nickel-base Superalloy. Superalloys, TMS.
Kapur, K.C., Lamberson, L.R., 1977. Reliability in Engineering Design. John Wiley & Sons, New York.
King, J.E., 1981. Crystallographic fatigue crack-growth in NIMONIC APl. Fatigue of Engineering Materials and Structures 4, 311–320.
Lerch, B.A., Jayaraman, N., Antolovich, S.D., 1984. A study of fatigue damage mechanisms in Waspoloy from 25-degrees-C to 800-degrees-C. Materials Science and Engineering 66, 151–166.
Li, K., Ashbaugh, N.E., Rosenberger, A.H., 2004. Crystallographic Initiation of Nickel-base Superalloys IN100 at RT and 538 °C Under Low Cycle Fatigue Conditions. Presented at Superalloys. Champion, Pennsylvania.
Mackenzie, J.K., 1958. Second paper on statistics associated with the random disorientation of cubes. Biometrika 45, 229–240.
Mackenzie, J.K., Thompson, M.J., 1957. Some statistics associated with the random disorientation of cubes. Biometrika 44, 205–210.
Manson, S.S., 1954. Behavior of materials under conditions of thermal stress. National Advisory Commission on Aeronautics: Report 1170. Lewis Flight Propulsion Laboratory, Cleveland.
McDowell, D.L., 1996. Basic issues in the mechanics of high cycle metal fatigue. International Journal of Fracture 80, 103–145.
McDowell, D.L., 1997. Multiaxial small fatigue crack growth in metals. International Journal of Fatigue 19, 127–135.
McDowell, D.L., 1999. Damage mechanics and metal fatigue: a discriminating perspective. International Journal of Damage Mechanics 8, 376–403.
McDowell, D.L., Berard, J.Y., 1992. A ΔJ-based approach to biaxial fatigue. Fatigue & Fracture of Engineering Materials & Structures 15, 719–741.
Miao, J., Pollock, T.M., Jones, J.W., 2007. Very high cycle fatigue behavior of nickel-based superalloy René 88DT at 593 °C. Presented at VHCF-4: Forth International Conference on Very High Cycle Fatigue, Ann Arbor, Michigan, USA, 2007.
Miao, J., Pollock, T.M., Jones, J.W., 2008. Fatigue Crack Initiation in Nickel-based Superalloy René 88 DT at 593 °C. Presented at Superalloys. Champion, Pennsylvania.
Miller, K.J., 1991. Metal fatigue. Past, current and future. Proceedings of the Institution of Mechanical Engineers. Part C: Mechanical Engineering Science 205, 291–304.
Miller, K.J., 1993. Materials science perspective of metal fatigue resistance. Materials Science and Technology 9, 453–462.
Miner, R.V., Gabb, T.P., Gayda, J., Hemker, K.J., 1986. Orientation and temperature-dependence of some mechanical-properties of the single-crystal nickel-base superalloy Rene-N4. 3: Tension–compression anisotropy. Metallurgical Transactions A: Physical Metallurgy and Materials Science 17, 507–512.
Nitz, A., Lagerpusch, U., Nembach, E., 1998. CRSS anisotropy and tension/compression asymmetry of a commercial superalloy. Acta Materialia 46, 4769–4779.
Pang, H.T., Reed, P.A.S., 2003. Fatigue crack initiation and short crack growth in nickel-base turbine disc alloys – the effects of microstructure and operating parameters. International Journal of Fatigue 25, 1089–1099.
Prasannavenkatesan, R., Zhang, J.X., McDowell, D.L., Olson, G.B., Jou, H.J., 2009. 3D modeling of subsurface fatigue crack nucleation potency of primary inclusions in heat treated and shot peened martensitic gear steels. International Journal of Fatigue 31, 1176–1189.
Pyrz, R., 1994. Correlation of microstructure variability and local stress-field in two-phase materials. Materials Science and Engineering A: Structural Materials Properties Microstructure and Processing 177, 253–259.
Randle, V., 2003. Microtexture Determination and Its Applications. Maney for the Institute of Materials, London.

Sadananda, K., Shahinian, P., 1981. Analysis of crystallographic high temperature fatigue crack growth in a nickel base alloy. Metallurgical and Materials Transactions A: Physical Metallurgy and Materials Science 12A, 343–351.
Sauzay, M., Jourdan, T., 2006. Polycrystalline microstructure, cubic elasticity, and nucleation of high-cycle fatigue cracks. International Journal of Fracture 141, 431–446.
Shenoy, M., Zhang, J., McDowell, D.L., 2007. Estimating fatigue sensitivity to polycrystalline Ni-base superalloy microstructures using a computational approach. Fatigue & Fracture of Engineering Materials & Structures 30, 889–904.
Shenoy, M., Tjiptowidjojo, Y., McDowell, D., 2008. Microstructure-sensitive modeling of polycrystalline IN 100. International Journal of Plasticity 24, 1694–1730.
Shyam, A., Torbet, C.J., Jha, S.K., Larsen, J.M., Caton, M.J., Szczepanski, C.J., Pollock, T.M., Jones, J.W., 2004. Development of Ultrasonic Fatigue for Rapid, High Temperature Fatigue Studies in Turbine Engine Materials. Champion, PA, United States.
Socie, D.F., 1993. Critical plane approaches for multiaxial fatigue damage assessment. In: McDowell, D.L., Ellis, R. (Eds.), Advances in Multiaxial Fatigue, ASTM STP 1191. American Society of Testing and Materials, Philadelphia, pp. 7–36.
Suresh, S., 1998. Fatigue of Materials, second ed. Cambridge University Press, Cambridge.
Swaminathan, S., Ghosh, S., 2006. Statistically equivalent representative volume elements for unidirectional composite microstructures. Part II: With interfacial debonding. Journal of Composite Materials 40, 605–621.
Swaminathan, S., Ghosh, S., Pagano, N.J., 2006. Statistically equivalent representative volume elements for unidirectional composite microstructures. Part I: Without damage. Journal of Composite Materials 40, 583–604.
Vincent, J.N., Remy, L., 1981. Temperature dependence of the pseudo-cleavage mechanism in the threshold regime of a super-alloy. Presented at Fatigue Thresholds: Fundamentals and Engineering Applications, Stockholm, 1981.
Westbrooke, E.F., Forero, L.E., Ebrahimi, F., 2005. Slip analysis in a Ni-base superalloy. Acta Materialia 53, 2137–2147.
Winter, A.T., Pedersen, O.B., Rasmussen, K.V., 1981. Dislocation microstructure in fatigue copper polycrystals. Acta Metallurgica 29, 735–748.
Zhang, J.X., Jiang, Y.Y., 2008. Constitutive modeling of cyclic plasticity deformation of a pure polycrystalline copper. International Journal of Plasticity 24, 1890–1915.
Zhang, M., Zhang, J., McDowell, D.L., Neu, R.W., 2006. Investigation of complex polycrystalline grain structures on fretting of duplex Ti-64 using 3D Voronoi tessellation. In: Ninth International Fatigue Congress (Fatigue 2006). Elsevier, Atlanta, GA.
Zhang, M., Zhang, J., McDowell, D.L., 2007. Micro structure-based crystal plasticity modeling of cyclic deformation of Ti–6Al–4V. International Journal of Plasticity 23, 1328–1348.
Zhang, J.X., Prasannavenkatesan, R., Shenoy, M.M., McDowell, D.L., 2009. Modeling fatigue crack nucleation at primary inclusions in carburized and shot-peened martensitic steel. Engineering Fracture Mechanics 76, 315–334.